ARTICLES

Translational Activation of the S_N2 Nucleophilic Displacement Reactions $Cl^- + CH_3Cl$ (CD_3Cl) → $ClCH_3$ ($ClCD_3$) + Cl^-: A Guided Ion Beam Study

Vincent F. DeTuri, Paul A. Hintz,† and Kent M. Ervin*

Department of Chemistry and Chemical Physics Program, University of Nevada, Reno, Nevada 89557

Received: April 30, 1997; In Final Form: June 24, 1997[⊗]

Guided ion beam tandem mass spectrometry techniques are used to examine promotion of the symmetric bimolecular nucleophilic substitution (S_N2) reaction $^{37}Cl^- + CH_3{}^{35}Cl \rightarrow {}^{35}Cl^- + CH_3{}^{37}Cl$ by translational energy. The translational energy threshold for this process is 45 ± 15 kJ/mol, well above the previously reported potential energy barrier height of 10−13 kJ/mol for the S_N2 transition state. The collisionally activated process involves conventional S_N2 back-side attack at the carbon atom, but passage over the barrier is impeded by nonstatistical dynamical constraints at collision energies just above the barrier. A significant secondary kinetic isotope effect is observed. The cross section for reaction with CH_3Cl is about 20% larger than for the reaction with CD_3Cl. At high energies, >410 ± 40 kJ/mol, diatomic Cl_2^- products are observed. The guided ion beam apparatus and data analysis procedures are described in detail.

I. Introduction

Bimolecular nucleophilic displacement (S_N2) reactions of halide ions with halomethanes

$$X^- + CH_3Y \rightarrow XCH_3 + Y^- \qquad (1)$$

have been the focus of many experimental and theoretical studies.[1,2] The S_N2 process, which results in inversion of the carbon center, is one of the most important organic reaction mechanisms. Strong solvent effects for these reactions in solution have prompted investigations of gas-phase S_N2 reactions to probe the intrinsic reactive behavior without solvent. It is now well established that the reactions proceed in the gas phase via a double-well potential.[1−4] The two wells correspond to loose ion−dipole complexes, $X^-\cdots CH_3Y$ in the entrance channel and $XCH_3\cdots Y^-$ in the product channel. The wells are separated by a potential barrier corresponding to the five-coordinate $[X-CH_3-Y]^-$ configuration.

Of particular interest is the gas-phase symmetric S_N2 exchange and inversion reaction,

$$Cl^- + CH_3Cl \rightarrow ClCH_3 + Cl^- \qquad (2)$$

This reaction system is small enough to be tractable by high-level theoretical methods, and the exchange of chlorine atoms can be followed experimentally by monitoring the $^{35}Cl^-$ and $^{37}Cl^-$ isotopes. The potential energy surface for reaction 2 is shown in Figure 1. The two minima are due to identical ion−dipole complexes with C_{3v} symmetry in the entrance and exit channels, separated by the transition state with D_{3h} symmetry. These geometries are shown in Figure 2. Previous experiments and theoretical calculations have probed various points on the potential energy surface of reaction 2, including the $Cl^-\cdots CH_3Cl$ complexation energy (E_C) and the height of the transition state barrier (E_B) relative to the energy of the reactants.

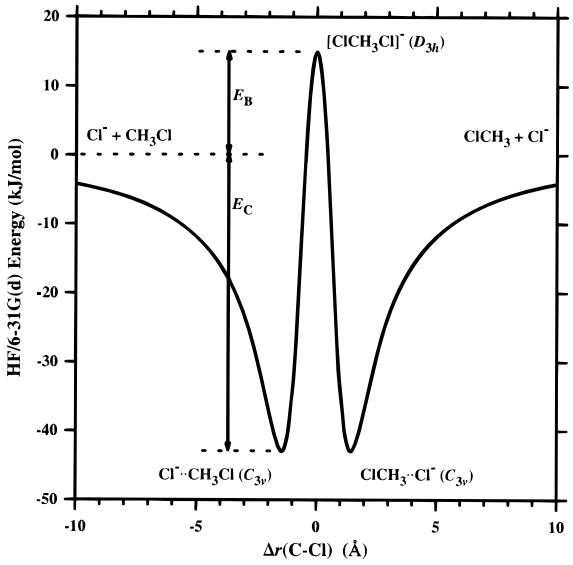

Figure 1. Double-well potential for reaction 2. The energy relative to reactants calculated at the HF/6-31G(d) level is plotted versus the difference between the two C−Cl bond lengths.

Experimental evidence of the barrier height comes from thermal rate measurements. The exchange rate was immeasurably slow in ion cyclotron resonance (ICR)[5] and selected ion flow tube (SIFT)[6] experiments, which suggested that the barrier is above the energy of reactants (i.e., $E_B > 0$). In later experiments using SIFT/drift tube techniques, Bierbaum and coworkers[7] measured a thermal rate coefficient for reaction 3 of $k = (3.5 \pm 1.8) \times 10^{-14}$ cm^3 s^{-1} at 300 K, which corresponds to a reaction efficiency of only one in 50 000 ion−molecule collisions.

$$^{37}Cl^- + CH_3{}^{35}Cl \rightarrow {}^{35}Cl^- + CH_3{}^{37}Cl \qquad (3)$$

* To whom correspondence should be addressed. E-mail: ervin@chem.unr.edu.

† Permanent address: Department of Chemistry and Biochemistry, La Salle University, Philadelphia, PA 19141.

⊗ Abstract published in *Advance ACS Abstracts,* August 1, 1997.

S1089-5639(97)01452-7 CCC: $14.00

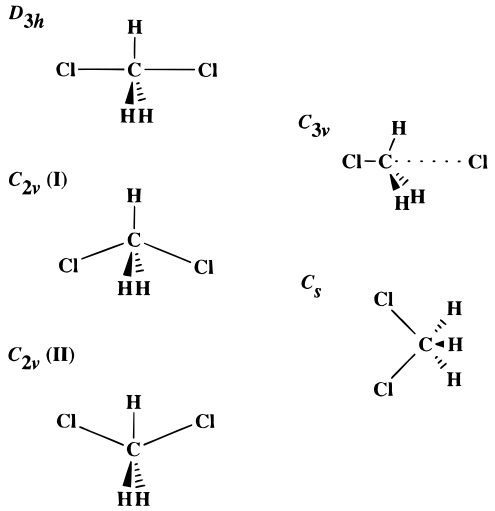

Figure 2. Structures of intermediates at several symmetries discussed in the text.

Using a simplified RRKM analysis, the authors[7] estimated the barrier height to be $E_B = 4 \pm 4$ kJ/mol (1 ± 1 kcal/mol) above the energy of the reactants. A barrier of $E_B = 13$ kJ/mol (3.1 kcal/mol) was found by Tucker and Truhlar[8,9] by modeling the experimental thermal rate coefficient using semiclassical canonical variational transition-state theory. Modeling the same experimental rate coefficient, Wladkowski and Brauman[10] obtained $E_B = 10$ kJ/mol (2.5 kcal/mol) using RRKM and microcanonical variational transition state theory, and Graul and Bowers[11] obtained $E_B = 12 \pm 1$ kJ/mol (0.12 ± 0.01 eV) using phase space theory. Thus, while the exact value varies depending on the statistical model used, a barrier height in the range $E_B = 10-13$ kJ/mol is consistent with the reported thermal rate. Classical trajectory calculations[12−18] indicate that reaction 2 exhibits strong *nonstatistical* behavior, placing statistical modeling of the rate in some doubt, however.

The barrier height and complexation energy have been calculated at various levels of theory,[8,9,13,14,16−28] as summarized in Table 1. The barrier height is sensitive to the level of the theory, with respect to both basis set size and inclusion of electron correlation. Recent high-level calculations give S_N2 barrier heights of $E_B \approx 12$ kJ/mol, in good agreement with the values inferred from the thermal rate coefficient.

Bierbaum and co-workers[7] measured the rate coefficients of reaction 3 as a function of mean collision energy in the SIFT/drift experiments. The observed rate coefficient is constant from thermal energies up to an apparent threshold of about 40 kJ/mol (0.4 eV) and then begins to rise exponentially. A deconvolution of the high-energy feature by Bierbaum and co-workers[7] yielded a threshold energy of 190 kJ/mol (2 eV). On the basis of an estimated energy of the $CH_3\cdots Cl_2^-$ complex of about 2 eV relative to $Cl^- + CH_3Cl$, Bierbaum and co-workers[7] attributed the threshold feature to front-side attack at the chlorine atom in chloromethane. Subsequent theoretical calculations[27,28] (Table 1) found a C_s saddle point on the potential energy surface with identical chlorine atoms corresponding to the front-side nucleophilic attack at the carbon atom, shown in Figure 2. The energy of that saddle point[27] is 194 kJ/mol, in good agreement with the reported drift tube threshold energy. However, in this work we show that the actual experimental threshold energy is much lower, that is, that the apparent agreement between the drift tube threshold energy and the calculated energy of the C_s saddle point is coincidental. The narrower energy distributions in our guided ion beam experiments allow a more precise analysis of the feature, which we believe involves a true S_N2 reaction mechanism.

Tucker and Truhlar,[9] Vande Linde and Hase,[12,13] and Billing[29] have developed multidimensional analytical potential energy surfaces for reaction 2 based on fits to ab initio calculations. The reaction kinetics and dynamics have been examined on these surfaces using transition state theory,[8,9,13,29] classical trajectories,[2,12,14−18] semiclassical reaction path dynamics,[29] and quantum scattering.[30] The trajectory studies by Hase and co-workers[2,12−14,16−18] have examined the effects of different modes of energy on the dynamics for complex formation and the S_N2 exchange reaction. They have found nonstatistical and non-RRKM effects for reaction 2. A phase space bottleneck limits transfer of energy between vibrational modes of the ion−dipole complex and internal vibrational modes of CH_3Cl, which is required for reaction to occur. Also, trajectories often exhibit multiple recrossings of the barrier, a breakdown of the transition state theory assumption. Hase and co-workers[12,14] also found that translational energy is ineffective in promoting the S_N2 reaction, which is an important consideration for the present experiments because we employ the translational activation of reaction 2. Both classical trajectory[12,14,17] and quantum scattering calculations[30] show that initial excitation of the C−Cl vibration gives a strong enhancement of the reaction probability.

The primary goal of the present study is to use guided ion beam methods to investigate the model S_N2 reaction system, reaction 3, as a function of collision energy. The theoretically predicted dynamical bottlenecks and inefficiency of translational activation suggest that the cross-section behavior should be particularly sensitive to the nature of the S_N2 potential energy surface. Guided ion beam methods allow studies at low collision energies under single-collision conditions with sensitive detection of products. The SIFT/drift results of Bierbaum and co-workers represent the only definitive previous observation of reaction 3.[5,7] In a scattering study of $Cl^- + CH_3Cl$ at relative energies greater than 3 eV, collisional electron detachment but no S_N2 products were observed.[31] Reaction 1 for endothermic systems, with X = Cl, Br, or I and Y = H or F, has been studied in beam/gas experiments,[32] but the observation of true S_N2 products was uncertain because the threshold energies were high enough for dissociative processes to be responsible (e.g., formation of $Y^- + CH_3 + X$).

We also examine reaction 4

$$^{37}Cl^- + CD_3{}^{35}Cl \rightarrow {}^{35}Cl^- + CD_3{}^{37}Cl \qquad (4)$$

to investigate kinetic isotope effects. Because the methyl group must deform to the planar geometry for passage over the S_N2 barrier, a significant secondary isotope effect might be expected. Truhlar and co-workers[9,33−35] predict an inverse kinetic isotope effect, $k_3/k_4 = k_H/k_D = 0.96$ for reaction 2 at 300 K, due mainly to vibrational frequency effects. Inverse kinetic isotope effects ($k_D > k_H$) have been observed[36−38] for the exothermic S_N2 reactions of Cl^- with CH_3Br and of F^- with CH_3X (X = Cl, Br, and I).

The complexation energy between Cl^- and CH_3Cl has been determined via equilibrium measurements using high-pressure mass spectrometry (HPMS)[39,40] and ion cyclotron resonance (ICR)[41,42] techniques. The experimental values agree well with theory (Table 1). To obtain an independent measurement of the complexation energy, we also have performed collision-induced dissociation experiments on the ion−molecule complex:

$$^{35}Cl^-\cdots CH_3{}^{35}Cl + Xe \rightarrow {}^{35}Cl^- + CH_3{}^{35}Cl + Xe \qquad (5)$$

A detailed description of our new guided ion beam tandem mass spectrometer used for these experiments and data analysis procedures is given in section II. Measured cross sections as a

TABLE 1: Relative Energies of Stationary Points (kJ/mol)[a]

species	experimental	method	ref	ab initio	method	ref
$Cl^- + CH_3Cl$ reactants	0.0			0.0		
$Cl^-\cdots CH_3Cl$	-39 ± 12[b]	CID	this work	−44.3	G2	this work
C_{3v} complex	-36 ± 1[b]	HPMS	39	−44.0 (−43.7[b])	G2(+)	26
	-51 ± 8[b]	ICR	41,42	−41	BH&HLYP	25
	−43.5[b]	HPMS	40	−44.4	MP4	28
				−43.1	NL-SCF	28
				−44.4	composite	24
				−38	CISD/DZDP	23
				−45.2	MP2/6-31G**	9
				−40.4	MP2/6-31++G**	22
				−43.1	HF/6-31G*	20
$[ClCH_3Cl]^-$	$<45 \pm 15$	empirical threshold law fit	this work	11.9	G2	this work
D_{3h} transition state	<41	phase space theory fit	this work	11.5 (9.8[b])	G2(+)	26
	4 ± 4	rate+RRKM	7	2.6	BH&HLYP	25
	13.0	rate[7]+semiclassical CVTST	9	7.5	MP4	28
	10.5	rate[7]+RRKM/μVTST	10	24	NL-SCF	28
	12 ± 1	rate[7]+PST	11	7.5	composite	24
				31	CISD/DZDP	23
				19	MP2/6-31G**	9
				32.1	MP2/6-31++G**	22
				15.0	HF/6-31G*	20
$[Cl_2CH_3]^-$				195.7	G2	this work
C_s saddle point				193.8	G2(+)	27
				215	MP4	28
				131	NL-SCF	28

[a] Energies relative to reactants at 0 K except as noted. [b] Enthalpy at 298 K.

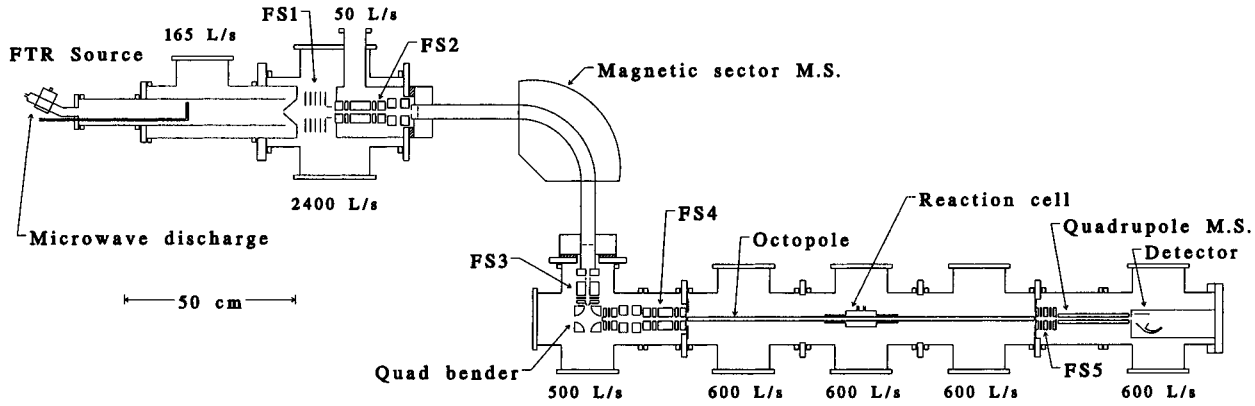

Figure 3. Guided ion beam tandem mass spectrometer.

function of collision energy are presented in section III, along with comparisons to previous experiments. The ramifications of the results for the S_N2 mechanism and potential energy surface are discussed in section IV. We employ ab initio calculations to clarify certain aspects of the potential energy surface and energetics for reaction 2. We also model the cross sections and the kinetic isotope effect to help elucidate the reaction mechanism. A summary of conclusions is provided in section V.

II. Guided Ion Beam Mass Spectrometry Experiments

A. Overview. A guided ion beam tandem mass spectrometer (GIB-MS) apparatus has been constructed for investigations of ion−molecule reactions and ion photodissociation processes. We have previously reported collision-induced dissociation experiments using this apparatus.[43,44] The basic concept is similar to GIB-MS instruments used by other groups, for example refs 45−50. Here we describe our instrument in detail, with emphasis on the unique design considerations that are pertinent to our specific applications. A diagram of the apparatus is presented in Figure 3. Briefly, ions are created in a flow tube reactor source, are mass-selected with a magnetic sector, and then interact with a neutral reactant gas in a radio frequency octopole ion beam guide. Ionic reaction products are collected by the beam guide, isolated from reactant ions by a quadrupole mass spectrometer, and detected.

B. Apparatus. 1. Flow Tube Reactor Ion Source. Ions are produced in a flow tube reactor (FTR), also known as a flowing afterglow.[51,52] The FTR was previously operated as an independent instrument for ion−molecule reaction kinetics studies[53−56] and will be only described briefly here. The stainless steel flow tube has a 7.3-cm inner diameter and a length from 0.5 to 1.7 m, depending on the number of tube sections used. For GIB-MS studies, shorter lengths may be used to increase the intensities of ions (which are lost via radial diffusion toward the walls) or longer lengths to provide more thermalizing collisions with the buffer gas. Helium is used as the buffer gas at a typical pressure of 0.5 mbar and a bulk flow velocity of 200 m s^{-1}. The FTR source provides a versatile means to make thermal ion species. Three methods of ion production in the flow tube have been utilized. For our studies of metal cluster anions,[43,53−56] a metal cathode discharge source[57,58] is used. A microwave discharge source[59,60] is used for producing nonmetal ions, such as Cl^- in the present work. An electron impact ionization source has also been used for diagnostic work.[53] Additional ions may be synthesized in the FTR by reactions

with neutral gases introduced via a ring inlet downstream of the discharge. In this work, CCl_4 vapor is used as the precursor gas to make Cl^- ions in the microwave discharge. Chloromethane (Matheson or Air Products, 99.5%) is added downstream to form $Cl^-\cdots CH_3Cl$ clusters.

2. Reactant Ion Selection. *Focusing Stages 1 and 2*. Ions are sampled from the flow tube through a 1-mm-diameter aperture in a conical nose cone (stainless steel coated with colloidal graphite) and are then extracted, accelerated, and focused by a series of aperture lenses in focusing stage 1 (FS1 in Figure 3). The ion energy origin is nominally fixed by the near-ground potential (0−3 V) of the nose cone. FS1 is similar to the lens system in our original FTR apparatus and is designed to minimize energetic ion collisions.[53] The pressure of the FS1 region is 1.5×10^{-4} mbar during operation of the flow tube. The ions are accelerated to 100−150 eV and focused through a 3-mm aperture that separates FS1 and FS2. Focusing stage 2 (FS2) is designed to accelerate the ions to the $V_{mag} = 1$ kV potential of the magnetic sector flight tube and to shape and steer the beam. A 5-element Heddle lens[61] design was selected for the accelerator because it can be used over a wide range of accelerations with well-characterized linear and angular magnifications. The lens apertures of these and all subsequent cylindrical lenses have diameter $d = 13$ mm and gaps of $d/10$. The five lens element lengths are $L_1 = L_5 = 25$ mm, $L_2 = L_4 = 13$ mm, and $L_3 = 66$ mm. The potential of the fifth element is fixed at $V_5 = V_{mag}$, while the others are adjustable up to 2 kV. The ion lens trains in FS2 and subsequent focusing stages are constructed from stacks of thin stainless steel plates fabricated by precision sheet metal punching. The lens plates are supported and aligned by four rods of poly(phenyl sulfide) polymer (Techtron PPS, Polymer Corp.), with aluminum spacers within lenses and insulating Techtron spacers between lenses.

Following the Heddle accelerator, an electrostatic quadrupole doublet lens[62,63] is used to transform the ion beam from cylindrical symmetry to a ribbon shape ideal for transmission through the slits of the magnetic sector. In the notation of Lu and Carr,[63] the pertinent dimensions are quadrupole rod physical length $D' = 24.6$ mm, effective length including fringe fields $D = 38.1$ mm, effective spacing $S = 0$, and distance to the entrance slit of the mass spectrometer $L = 17.8$ mm. The quadrupole rods have circular cross section, with the ratio of rod radius ($r = 13.6$ mm) to distance from the ion beam axis to the inner surface ($r_0 = 11.8$ mm) chosen to approximate an ideal hyperbolic potential.[64] Vertical and horizontal deflection potentials are superimposed on the second quadrupole to provide steering control. Use of the quadrupole doublets improves transmission through the magnetic sector by a factor of 2 or more.

Magnetic Sector Mass Spectrometer. A magnetic sector momentum analyzer was chosen for the initial mass spectrometer because it maintains high ion beam quality; a dynamic quadrupole mass filter would introduce energy broadening. The magnetic sector was taken from a commercial double focusing instrument (Varian MAT 311A). The 90° sector has a radius of 20.3 cm, and a m/z range up to 3600 daltons for a flight tube potential of 1 kV. Fixed 1-mm entrance and exit slits are used. Because the FTR source operates at ground potential, the flight tube must be floated at high voltage. The flight tube is insulated from the magnet poles by high dielectric paper (0.25-mm-thick "fish paper", Small Parts, Inc.) and from the adjacent vacuum chambers by nylon flanges. With water cooling of the electromagnet, the magnetic field is sufficiently stable in current-control mode, although field control is also available using a Hall probe feedback circuit. The measured mass resolution of the magnetic sector is about 200 ($M/\Delta M$, 10% valley) at 1000 daltons.

Focusing Stage 3 and Quadrupole Bender. Following the second slit of the magnetic sector, the ions enter a series of rectangular tube lenses (FS3) that transfer the beam to an electrostatic quadrupole bending lens.[65] The 90° bend in the ion beam is included primarily for convenience in passing a laser beam through the interaction region coaxially with the ion beam. Because both the magnetic sector and the bending lens have planar symmetry, the ribbon-shaped beam is maintained through this region. The rectangular tube lenses have 13 mm × 44 mm apertures. FS3 is primarily a field-free region but includes horizontal and vertical deflectors for steering adjustments and a single Einzel lens before the bender.

The quadrupole bending lens rods have quarter-circular cross sections of radius $r = 28.8$ mm and distance $r_0 = 25.1$ mm from center to pole face, giving gaps of 9 mm at the entrance and exit faces. Quadrupole bending lenses have been widely used since their conception by Zeman,[65] who described the use of shims combined with rods of quarter-circular cross section to approximate the ideal hyperbolic field. Others[66,67] have simply used rods of quarter-circular cross section. On the basis of SIMION[68] model potential and trajectory calculations, we concluded that nonideal dispersion of the ions through the bender is caused not by nonhyperbolic fields but rather primarily by the fringing fields at the entrance and exit apertures. Several methods have been proposed to reduce the effects of fringing fields at the apertures of condensers, primarily for electrostatic charged-particle energy analyzers. These methods include field termination lenses,[69] aperture plates,[70] grids,[71] and oblique injectors.[72] We have designed simple oblique injector and extractor lenses similar in principle to the design of Ballu.[72] The fringing fields are terminated by V-shaped injector plates at the center potential of the quadrupole. In the limit of a sharp V with no gap, the distortion of the field near the aperture would be largely eliminated. The chosen obliqueness (45° half-angle) and gap (4.8 mm) are compromises among the considerations of ideal field, transmission of the ion beam, and fabrication ease. SIMION[68] trajectory calculations show the terminators substantially decrease the angular dispersion of the ions, compared with other approaches.[69,70] Because some dispersion is unavoidable, rectangular tube Einzel lenses (6.4-mm center lens length, 1.3-mm gaps) are placed before and after the quadrupole bender to provide focusing corrections.

Focusing Stage 4 and Deflector. Following the bender lens, the ion beam is reconverted to cylindrical symmetry by a second electrostatic quadrupole doublet lens and then decelerated by a five-element Heddle lens. The dimensions of these lenses are identical with those in FS2, in reverse order. For time-of-flight measurements of the ion energies and for pulsed ion beam experiments described below, a deflector is incorporated into the middle lens of the Heddle decelerator to gate the beam prior to the interaction region. For pulsed beam operation, the two sides of the deflector are connected to opposite polarities of a ±100 V symmetric pulse with the baseline voltage at the lens focusing potential. A pulse/delay generator (Berkeley Nucleonics Model 500A) drives a floating high-voltage pulse circuit adapted from a published design.[73,74] The rise and fall times of the deflector pulse are less than 100 ns, and those of the resulting ion pulses are shorter than the 2 μs resolution of our multichannel scaler ion detector.

3. Interaction Region. *Octopole Ion Beam Guide*. In the interaction region the ions are guided by an octopole radio frequency ion trap, which provides a radial effective potential

well for highly efficient collection of ionic reaction products. The theory and operation of radio frequency multipole ion traps is the subject of a recent thorough review.[75] Our octopole is composed of eight 3.2-mm-diameter molybdenum (Schwarzkopf Corp.) rods arrayed on a 11.6-mm-diameter circle. This geometry provides the $r/r_0 = 0.37$ ratio, where r is the electrode radius and r_0 is the distance from the center axis of the octopole to the pole faces, that best approximates an 8-fold hyperbolic potential with rods of circular cross section.[76] The octopole rods are 101.4 cm long, longer than necessary for the cross-section measurements, but designed to enable future time-of-flight measurements of ion photodissociation lifetimes in experiments akin to those of Jarrold and co-workers.[47] The octopole injector lens (final element of the FS4 decelerator) and extractor lens (first element of FS5) have 4.8 mm apertures, and protrude 1.5 mm into the ends of the octopole to help shield ions from fringing fields. The resulting length of the octopole region is $L = 101.1$ cm. The octopole rods are mounted on and aligned by four Techtron disks; the rods themselves provide the structural support.

The radio frequency (rf) potentials are provided by a resonant *LC* circuit driven by a gate-able function generator (Hewlett-Packard 8165A), amplified as required (ENI Model 2100L), and impedance-matched with an amateur radio antenna tuner/power meter (MFJ Model 949E). The octopole itself is the capacitor ($C \approx 200$ pF) and the inductor (L) is a multiturn formed coil (Barker & Williamson) mounted immediately outside the vacuum chamber. A frequency of 3.3 MHz ($L \approx 10$ μH) and amplitude of 80−100 V on the rods was used for the present work; a lower frequency of 1.0 MHz ($L \approx 130$ μH) has been used for higher-mass metal cluster ions. Variable, high-voltage air capacitors (10−30 pF, Oren Elliot Prod.) connected to each side of the octopole circuit are used to balance the rf amplitudes on the two phases.

Gas Cell. Midway along its length, the octopole passes through a gas reaction cell. The body of the gas cell (89 mm long × 50 mm diameter) and two extension tubes (57 mm long × 17 mm diameter) are stainless steel, while the end walls are Techtron disks mounted on the octopole rods. The extension tubes are designed to limit gas conductance from the cell.[45] Gases are introduced via Teflon tubing from a leak valve (Granville Phillips 203). The effective cell length is estimated to be 14.6 cm (assuming a trapezoidal pressure profile[45]). Gas cell pressures of $(3-20) \times 10^{-5}$ mbar are measured with a capacitance manometer (MKS Baratron 127AA). To measure lower pressures precisely for cross-section measurements, a calibration between the capacitance manometer and the octopole chamber ionization gauge is used. A pressure difference ratio of about 90:1 can be maintained between the gas cell and the octopole chamber. For measurement of background gas reactions,[45] the gas flow may be switched to the main chamber, creating the same measured background pressure as when the flow is directed to the cell. The effective path length for background reactions is about 1 m, much longer than the gas cell path length, leading to a measured foreground/background ion intensity ratio of about 15:1.

4. Quadrupole Mass Spectrometer Detector. Ions are extracted from the octopole and injected into the quadrupole mass spectrometer by a series of five cylinder lenses in focusing stage 5 (FS5). The quadrupole mass spectrometer (Extrel, 9.5-mm-diameter rods, 20.6 cm long, oscillator frequency 1.2 MHz) is the same as used in our previous FTR instrument.[53] In its normal operating mode, the quadrupole mass filter has a mass range up to 1500 daltons. This range was chosen for our work on transition-metal cluster ions. A high mass range for quadrupole mass spectrometers requires relatively small-diameter rods, low frequency, and high rf amplitudes. The optimal parameters for lower masses are larger rods and higher frequency. An alternative to these changes in the quadrupole and power supply is to employ the second stability region of the Mathieu stability diagram for quadrupole mass spectrometers instead of the usual first region.[77] (The "second" stability region is also sometimes termed region III.[78]) Operation in the second stability region requires only a change in the ratio of rf amplitude (V_{rf}) to dc potential (U_{dc}) on the quadrupole rods: $V_{rf}/U_{dc} \approx 6$ for the first stability region and $V_{rf}/U_{dc} \approx 2$ for the second.[77] Figure 4 presents mass spectra of the $^{37}Cl^-$ ion beam and $^{35}Cl^-$ product ions from reaction 3. The second stability region provides superior discrimination between adjacent masses compared with the first stability region, for low masses. Using the second stability region, we can eliminate overlap between the two chloride isotopes (>10^6:1 abundance sensitivity) while keeping ion transmission high by setting the resolution as low and the axial ion energy as high (45−65 V for this work) as practical. In the second stability region mode, the mass range of the quadrupole is limited by the dc power supply to below 140 daltons.

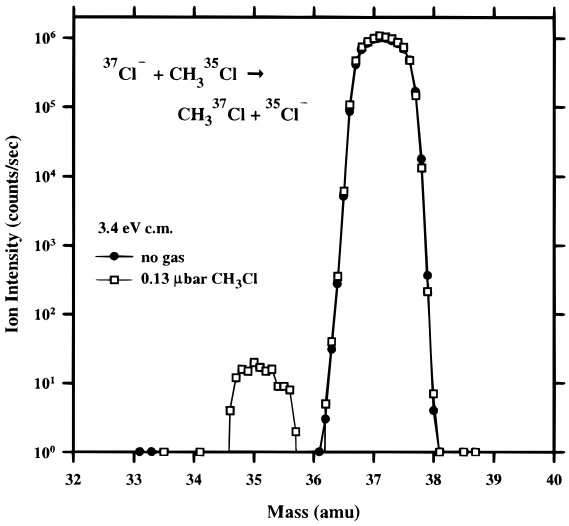

Figure 4. Mass spectra using the second Mathieu stability region of the quadrupole mass spectrometer. The $^{37}Cl^-$ isotope is selected with the initial magnetic sector mass spectrometer, and the quadrupole mass spectrometer is scanned to separate reactant ions from $^{35}Cl^-$ product ions from reaction 3 at 3.4 eV c.m. Mass spectra are shown with (open symbols) and without (solid symbols) CH_3Cl in the gas cell. Each point represents a counting time of 1 s.

Ions are detected by a collision dynode/channeltron multiplier (Galileo 4870E) operated in negative-ion pulse counting mode. Signal pulses are processed by a preamplifier (EG&G Ortec VT120) and leading-edge threshold discriminator (Canberra 2126). The pulses are counted by a multichannel scaler computer board (Canberra Accuspec FMS) with 2-μs minimum dwell time, used in nontiming applications as a single channel scaler.

5. Data Acquisition System. The guided ion beam apparatus is controlled by a personal computer (Intel 80386/387 processor). Hardware control and data acquisition functions are provided by 12- and 16-bit analog-to-digital and digital-to-analog converters and digital outputs. The computer measures the pressures and flow rates of gas for the flow tube reactor source, the octopole gas cell pressure from the capacitance manometer, and the octopole chamber pressure from an ion gauge. The octopole dc potential, the octopole rf amplitude, the octopole injector and extractor lens potentials, and the mass settings for the magnetic sector and quadrupole mass spectrom-

eters are computer-controlled. A menu-based computer program written in C provides major functions including an ion count rate meter, quadrupole and magnetic sector mass scans, and ion energy scans for specific reactant and product ion masses, each with graphical display of the data. Nonautomated functions include only gas flow rates (controlled manually with variable leak valves) and potentials of ion focusing lenses that need not vary with ion interaction energy.

C. Experimental Protocols. 1. Ion Energy Measurement. In the stationary target approximation, the conversion between laboratory ion energy (E_{lab}) and the relative collision energy in the center-of-mass (c.m.) frame (E_{cm}) is given by

$$E_{cm} = E_{lab}M_{gas}/(M_{ion} + M_{gas}) \quad (6)$$

where M_{ion} is the ion mass and M_{gas} is the reactant gas mass.[45] The laboratory ion energy is nominally the difference between the near-ground potential of the ion source and the dc potential of the octopole. The laboratory ion energy zero and the energy spread are determined by retarding potential analysis (RPA), using the octopole as the retarder, by measuring the ion beam intensity while sweeping the octopole dc bias voltage through the nominal zero potential.[45] The ion energy zero is strongly affected by the potential on the nosecone aperture of the flow tube, where the ions undergo their last collisions. Therefore, the nosecone voltage is kept as near ground potential (same as the flow tube) as possible and is not adjusted during reaction scans. The estimated random error in the RPA ion energy zero measurement is ±0.05 eV. Typical ion energy spreads for the flow tube reactor ion source are $E_{fwhm} = 0.10-0.25$ eV fwhm (full width at half-maximum), based on Gaussian fits to the RPA derivative curves.

We also employ time-of-flight (TOF) measurements of the ion energy. For this purpose, the ions are pulsed at the deflector in FS4. The time-of-arrival distributions at several ion energies are shown in Figure 5a for an ion pulse width of 10 μs. Figure 5b shows a plot of the peak times-of-arrival versus nominal octopole dc potential, which is fit to the electrostatic equation,

$$t(U_{oct}) = t_0 + L_{eff}M_{ion}^{1/2}\Big/\left((eU_{oct} - eU_0) + \left[(eU_{oct} - eU_0)^2 + \frac{3E_{fwhm}^2}{4\ln 2}\right]^{1/2}\right)^{1/2} \quad (7)$$

where t is the peak time-of-arrival after the ion pulse trigger, U_{oct} is the nominal octopole dc potential, U_0 is the actual ion source potential, e is the electron charge, t_0 is the sum of the time the ions spend outside the octopole and any electronic delays, L_{eff} is the effective length of the octopole time-of-flight region, M_{ion} is the ion mass, and E_{fwhm} is the ion beam energy spread measured by retarding potential analysis. The extra term containing E_{fwhm} in the denominator of eq 7 arises from the transformation between peak time-of-arrival and mean energy for an assumed Gaussian ion energy distribution. A nonlinear least-squares fit of eq 7 is used to find U_0, t_0, and L_{eff}. The effective length L_{eff} is typically 0.5−2% less than the physical octopole length $L = 1.011$ m because of field penetration from the injector and extraction lenses. The random uncertainty of the time-of-flight measurement of U_0 is ±0.1 eV.

The TOF measurements yield ion energies that are systematically 0.05−0.2 eV (lab) higher than those found by retarding potential analysis, sometimes outside the mutual random uncertainties. The deviation tends to become worse when the octopole rods are contaminated. The retarding potential method is subject to error if there are local energy barriers in the octopole

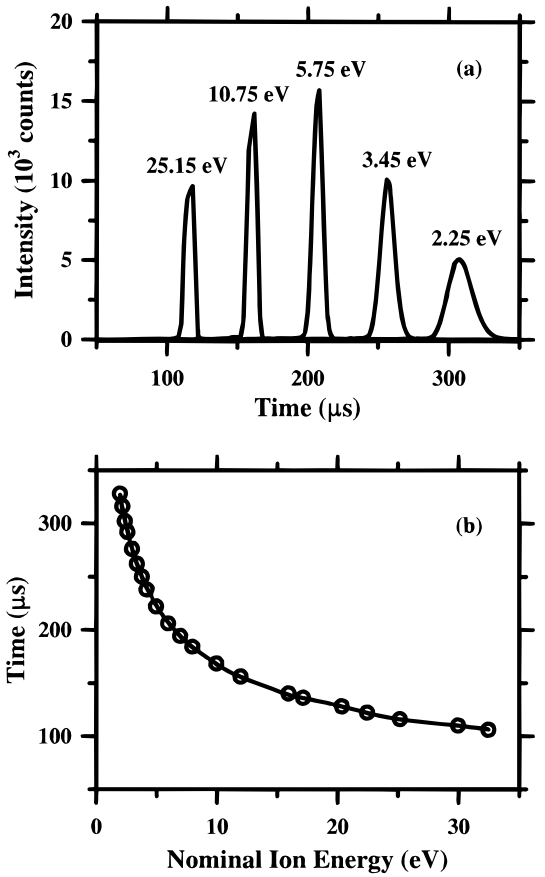

Figure 5. Time-of-flight measurement of the ion energy. (a) Time-of-arrival distributions for selected laboratory ion energies, with an ion beam pulse width of 10 μs. (b) Peak times-of-arrival versus nominal octopole dc potential (circles) and fit to eq 7 (line).

that block the transmission of the lowest energy ions. Local energy barriers may arise from nonuniform surface potentials on the rods, from foreign particles, or from insulating coatings of reagent gases that can charge up.[75,79] The ion injection focusing at the near-zero energies required for retarding potential analysis might convert some axial ion energy into radial motion, which would also give an apparent energy offset. The TOF measurement is less susceptible to local energy barriers because it averages over the whole length of the octopole, but it is subject to other errors. In particular, SIMION[68] simulations indicate the effective length of the flight region in eq 7 actually varies with nominal ion energy because of differential field penetration from the injection and extraction focusing potentials. Diagnostic measurements of reaction thresholds for reaction 5 and some proton-transfer calibration reactions studied under various conditions over a period of months indicate that the RPA measurements are statistically more reproducible (lower standard deviations of the threshold energies) than are the TOF measurements. Furthermore, the absolute reaction threshold energies determined using the TOF method are directly correlated with the deviation from the RPA energy zero, which implies that the TOF measurement is primarily responsible for the systematic errors. Therefore, the RPA values measured before and after each scan are used for the ion energy zero determination, with an estimated overall uncertainty of 0.1 eV (lab). Daily TOF measurements are used to check for gross errors in the retarding potential analysis due to local barriers from dirty rods. If the deviation between the retarding potential and TOF measurements is found to exceed about 0.2 eV, the octopole rods are cleaned.

2. Cross Section Measurement. At a given collision

energy, the total reaction cross section, σ_{tot}, is given by the incident ($I_{R,0}$) and transmitted (I_R) reactant ion intensities (counts per unit dwell time) according to the Beer's law relationship

$$I_R = I_{R,0} \exp(-\sigma_{tot} nl) \tag{8}$$

where n is the gas density and l is the effective path length. In practice, $I_{R,0}$ is determined from

$$I_{R,0} = I_R + \Sigma I_P \tag{9}$$

where the sum is over all the product ion intensities I_P for all reaction channels. Individual product channel cross sections are given by

$$\sigma_P = \sigma_{tot} (I_P/\Sigma I_P) \tag{10}$$

To measure cross sections as a function of collision energy, a scan is taken over the ion energy (octopole dc potential) range of interest, with ions at the reactant mass and each product mass counted for predetermined dwell times (typically 0.1−2 s) at each energy, at a fixed gas cell pressure. For the measurement of small cross sections, longer ion counting dwell times are used for products than for the reactant ions to maximize the overall signal-to-noise for a given total scan time. Ion counts due to background signals of various types are subtracted by taking background scans with the reactant gas directed to the octopole chamber instead of the gas cell, as described previously.[45] For signal averaging, alternating foreground and background scans are accumulated for many (5−50) cycles. Equations 9 and 10 are valid as long as all product ions are collected (which may usually be assumed because of the high collection efficiency of the octopole) and in the absence of pressure-dependent secondary reactions or processes. Multiple collisions can have a magnified effect in the threshold region of an endothermic reaction, either by promoting dissociation in collision-induced dissociation[80] or by stabilizing an intermediate ion-neutral adduct in a bimolecular reaction. Therefore, all cross sections are measured at three or more pressures in the range (3−20) × 10^{-5} mbar and extrapolated to zero pressure by a least-squares linear regression. This extrapolation ensures that the reported cross sections are rigorously in the single-collision limit.

Random errors for cross sections measured at each energy and pressure are determined by propagating the statistical (Poisson) counting uncertainty, $\sigma_I = I^{1/2}$, for each accumulated ion intensity through the background subtractions and eqs 8−10. The random errors for the gas cell pressure determination (typically ±1 × 10^{-5} mbar) are obtained from the capacitance manometer/ion gauge calibration linear regression, and the estimated temperature variation (±0.2 K) is included. No uncertainty in the gas cell length is included because that error would systematically affect all results. The propagated estimated standard deviations are used to weight the cross-section values in the least-squares linear regressions in the extrapolation to zero pressure. The final uncertainty in the reported cross section is obtained as the estimated standard deviation of the zero-pressure intercept from the linear regression extrapolation.[81] The error bars given in plots of cross-section measurements are these statistical uncertainties, which represent realistic relative uncertainties of cross sections at different energies. The accuracy of the absolute magnitudes of our cross sections is limited by the determinations of the true effective path length, the pressure, the temperature, and possible mass discrimination of the ion detector. We estimate our cross section absolute magnitudes are accurate to within ±50%.

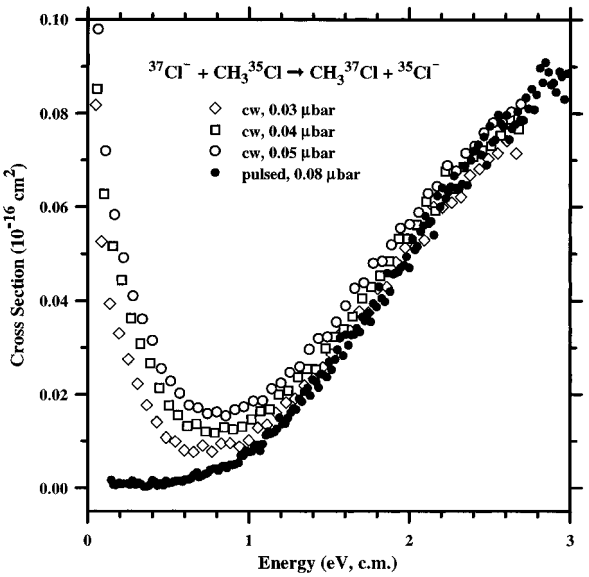

Figure 6. Cross sections for reaction 3 using a continuous (cw) ion beam show a pressure-dependent artifact at low energies due to trapped ions (open symbols). The pulsed ion beam mode (solid symbols), with $\tau_1 = \tau_2 = 1.5$ ms, largely eliminates the artifact. See text for details.

3. Pulsed Ion Beam and Gated rf Field Modes. An ion in the octopole experiences a field-free region except for the radial effective trapping field. Therefore, ions in the octopole at the instant the dc voltage is changed retain their original energy, different from the new energy setting. To clear the octopole of such ions, the rf octopole potential is gated off for a short period (0.05−0.2 ms) each time the energy is changed. With the rf field off, the ions quickly drift out of the trapping region.

A related experimental issue is the trapping of ions axially in the octopole. At low energies, ions that undergo a collision may have their forward momentum partially converted into radial motion. If there are small local energy barriers in the octopole (see section II.C.2), such ions can become trapped in the octopole. Trapped ions can be observed by switching the ion beam off and measuring the ion intensity as a function of time; some of the trapped ions leak out of their local energy wells and drift to the end of the octopole to the detector. The apparent trapping time and number of trapped ions is dependent on uncontrolled experimental conditions. At near-zero nominal ion beam energies, we have observed steady-state intensities of trapped ions of 0.008−0.03% of the ion beam intensity, with decay time constants of 0.2−3 s. With increasing octopole chamber background pressure, the concentration of trapped ions tends to increase while the apparent decay times become shorter.

Trapped ions can give rise to artifact reaction products at low collision energies. Figure 6 shows the pressure dependence of the apparent cross section for reaction 3 measured in the presence of trapped ions. While the threshold feature above 1 eV is not pressure dependent, an apparent "exothermic" channel at low energies is pressure dependent and does not cleanly extrapolate to zero at zero pressure. This low-energy feature varied in magnitude from day to day. The magnitude of the feature definitely correlates with the observation of trapped ions, though not always proportionately. The phenomenon tends to become worse at higher rf potential amplitudes on the octopole. Other possible causes of the low-energy artifact were tested by diagnostic experiments. Specifically, we tested various octopole cleaning protocols, trapping for impurities such as HCl or Cl_2 (which react rapidly[6] with Cl^-) by passing the CH_3Cl through activated basic alumina, changing the background pressure in

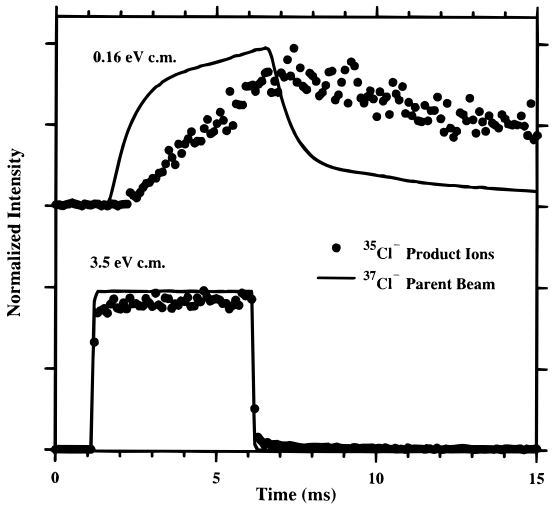

Figure 7. Time-of-arrival distributions for reactant and product ions for reaction 3 at collision energies of 0.16 eV c.m (upper plot) and 3.5 eV c.m. (lower plot) at a gas cell CH_3Cl pressure of 0.2 μbar. At the higher energy, the reactant and product ions mimic the 5-ms-long square pulse on the ion deflector gate. At the low energy, the rise and fall times of the reactant ions are less sharp because of the ion energy spread. The product ions build up slowly and then persist after the end of the pulse, which is characteristic of reactions due to trapped ions (see text).

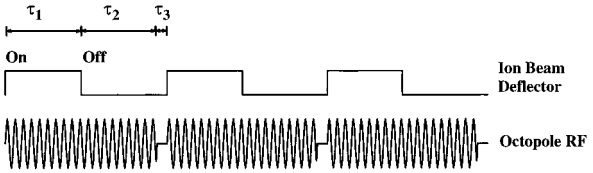

Figure 8. Schematic timing sequence for the pulsed ion beam mode of operation: (top) ion beam deflector pulse and (bottom) amplitude of the radio frequency trapping field on the octopole.

the octopole region or focusing stages 1−4, re-aligning or misaligning the octopole rods, and using stainless steel, molybdenum, or graphite-coated octopole rods. None of these procedures resulted in a reproducible change of the low-energy feature or of the trapped ions.

False observation of products results from trapped ions because they can undergo many cycles of the rf trapping fields and multiple collisions with reactant gas. If a collision occurs near the octopole rods during a high-voltage phase of the rf cycle, the trapped ion can be accelerated to a higher energy and become reactive. Our solution to the trapped ion problem is to operate the ion beam in a pulsed mode, following each pulse by a short period with zero rf field to clear the octopole. This procedure works because there is an induction period for trapped ions to react, as shown in Figure 7. For reaction 3 at low collision energies, product ions begin to appear about 1 ms after the beginning of the reactant ion beam pulse. The ions responsible for this product signal have been trapped for times corresponding to at least 10^3 rf cycles and 10^2-10^3 collisions. The chosen pulsed-beam sequence is illustrated in Figure 8, with an ion pulse duration of τ_1 (corresponding to the width of the "open" pulse on the deflector in FS4). The rf field remains on for an additional time τ_2 for the ions near the end of the pulse to pass through the octopole and be detected, including product ions that might be scattered with slower forward laboratory velocities than the reactant ion beam. Then the rf field is gated off for τ_3 to clear the octopole of all trapped ions before beginning a new cycle. The reaction cross section measured using this pulsing sequence is shown in Figure 6; the low-energy artifact is largely eliminated. Pulsing the ion beam establishes a lower limit on the collision energy for collecting product ions, because very slow product ions might not reach the detector before the rf amplitude is switched off. Under the conditions in Figure 6, $\tau_1 = \tau_2 = 1.5$ ms and $\tau_3 = 0.2$ ms, the lower energy limit is 0.14 eV c.m. for reaction 3, calculated assuming that the slowest product ions have the center-of-mass velocity (i.e., neglecting backscattering).

We have also observed the trapped ion phenomenon in other systems, including CID of metal cluster ions and proton-transfer reactions, but reaction 2 is especially susceptible, partly because of its relatively low threshold energy. Circumstantial evidence suggests that the problem is exacerbated by sticky or corrosive reagent gases used in the gas cell, *including* chloromethane. Our octopole design may be particularly susceptible to the trapped ion phenomenon because it is long (1 m), with large surface area and therefore more opportunity for nonuniform surface potentials on the rods. We routinely check for trapped ions and use the pulsed ion mode of operation whenever necessary.

D. Threshold Energy Analysis. No fully validated or generally applicable theory is available to predict threshold behavior as a function of translational energy. We follow other workers in the field and use an empirical threshold law given by

$$\sigma(E) = \sigma_0(E - E_{th})^N/E \qquad (11)$$

where E is the relative collision energy, E_{th} is the threshold energy, σ_0 is a scaling factor, and N is a variable parameter. This threshold law (eq 11) has been used extensively to determine threshold energies.[46,82−84] Other investigators[85−90] have discussed the validity of the threshold law, which for $N = 1$ corresponds to the line-of-centers hard-sphere collision model.[91] Values of $N = 0.5$, 1.5, 2.0, or 2.5 have been derived[85−87,89,91,92] for various other models and reaction types. Until firm theoretical predictions can be made for the cross section threshold behavior for a given reaction mechanism, we simply use eq 11 with N as an adjustable parameter.

Equation 11 is modified by summing over the experimental vibrational and rotational energy levels of the reactants,[82,90,93] yielding

$$\sigma(E) = \sigma_0 \sum_i g_i P_D(E,E_i,\tau)[E + E_i - E_{th}]^N/E \qquad (12)$$

where E_i is the internal energy of reactant state i with fractional population g_i and $P_D(E,E_i,\tau)$ is the detection probability considered below. The inclusion of the sum over internal energy levels in the numerator in eq 12 assumes that the total energy is available for promoting chemical reaction. In the absence of a reverse activation barrier, the threshold energy E_{th} can therefore be equated with the zero-temperature reaction endoergicity, $E_{th} = \Delta U_0 = \Delta H_0$. Because of the strong ion/induced-dipole long-range attractive potential, ion−molecule reactions often have no activation energy in excess of the overall endoergicity.[83,94] The thermoneutral S_N2 reaction investigated in this work is an exception because of the energy barrier at the tight transition state for nucleophilic displacement; its threshold behavior may be different from that for endoergic ion−molecule reactions with loose transition states near the product channel. Postponing that issue, we describe now our general protocol for determining threshold energies from zero-pressure cross section data using eq 12.

We generate a model function of the form of eq 12, using vibrational and rotational frequencies for the reactants taken from the literature or estimated and including electronic energy

levels if populated. Rovibrational state densities can be very high; therefore, the summation in eq 12 is condensed[93] by integrating over the rovibrational state densities calculated using the Beyer−Swinehart direct count algorithm.[95−97] For collision-induced dissociation processes, a final correction to eq 12 is necessary to correct for kinetic shifts due to the limited time window for dissociation before detection. Collision events that transfer just enough energy for dissociation will not be registered if the activated molecule does not dissociate in the time-of-flight from the gas reaction cell to the quadrupole mass spectrometer. We account for this effect by using a statistical RRKM calculation of the dissociation probability combined with a simple collision energy transfer model to calculate $P_D(E,E_i,\tau)$ in eq 12, as described in detail elsewhere.[44,93] Finally, eq 12 is convoluted over the experimental translational energy distributions[98−100] as described previously.[45]

After inclusion of these effects, the adjustable parameters, σ_0, N, and E_{th}, are obtained by a nonlinear least-squares fit of eq 12 to the data using a modified version of the Marquardt optimization algorithm.[81] The cross-section data are weighted according to their estimated statistical standard deviations, calculated as described above. The statistical uncertainties of the parameters are given by the least-squares optimization based on the curvature of χ^2 (sum of squared residuals) with respect to the parameter. (Note that to obtain correct parameter uncertainty estimates from the Marquardt algorithm, true standard deviations must be used to weight the data and the search parameter[81] F_λ must be set to zero.[101]) In reporting error limits for E_{th}, we use this estimated statistical uncertainty of the fit as one component of the error. Other components are the uncertainty of the ion energy determination, partial modeling error estimated by using different energy ranges for the fit (since the range of validity of eq 11 at energies above threshold is uncertain), the reproducibility of threshold energies from data taken under different conditions and at different times (estimated standard deviation), uncertainties due to the vibrational frequencies and other molecular parameters used in the model, and uncertainty in the experimental time window for the RRKM correction for CID reactions. The latter two are estimated by repeating fits with these input parameters varied to reasonable extremes. We take the root-mean-square average of these estimated uncertainties (which assumes they are independent), then double them to give an approximate 95% confidence level estimate of the error limits. Although estimating some of these components of the uncertainty involves qualitative judgments, we believe the resulting error limits for E_{th} represent reasonable, conservative, and consistent estimates of random error. Systematic errors due to deficiencies of the threshold model are not included. Most of the data analyses are performed using a recently modified 32-bit version of the Crunch FORTRAN program.[102]

III. Results

A. $Cl^- + CH_3Cl$ Reaction. 1. Measured Cross Sections. The single-collision cross section for the reaction of $^{37}Cl^-$ with CH_3Cl as a function of the relative collision energy in the center-of-mass frame is shown in Figure 9. An expanded plot of the threshold region for reaction 3 is shown in Figure 10. The mass-37 isotope of Cl^- is selected by the initial magnetic sector mass spectrometer, but chloromethane (Matheson or Air Products, 99.5%) is used in natural isotopic abundance (75.8% ^{35}Cl, 24.2% ^{37}Cl). The chloride exchange reaction can be detected only for $CH_3{}^{35}Cl$ by formation of $^{35}Cl^-$. At low energies, $^{35}Cl^-$ is produced with an apparent threshold energy of about 0.5 eV. At higher energies, we also observe the diatomic products $^{35}Cl^{37}Cl^-$ and $^{37}Cl_2^-$. In Figure 9, the magnitudes of the apparent cross sections for formation of $^{35}Cl^-$,$^{35}Cl^{37}Cl^-$, and $^{37}Cl_2^-$ have *not* been adjusted for isotopic abundances of CH_3Cl. $^{35}Cl^{37}Cl^-$ and $^{37}Cl_2^-$ are observed in the expected 3:1 ratio. In all other plots, the apparent cross section for reaction 3 has been scaled by a factor of 1.32 to correct for the partial pressure of the $CH_3{}^{35}Cl$ isotopomer. We also performed some experiments on $^{35}Cl^- + CH_3Cl$, the reverse of reaction 3, and confirmed that the apparent cross sections for formation of $^{37}Cl^-$ differ in magnitude by the expected 3:1 isotopic ratio but are otherwise identical.

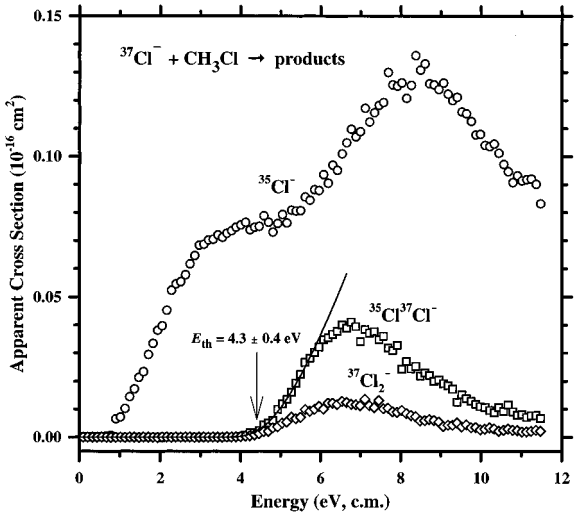

Figure 9. Apparent cross sections for the reaction of $^{37}Cl^- + CH_3Cl$ as a function of energy in the center-of-mass frame. Products shown are $^{35}Cl^-$, $^{35}Cl^{37}Cl^-$, and $^{37}Cl_2^-$. The cross sections are *not* scaled to account for the natural isotopic abundance of ^{35}Cl (74.8%) and ^{37}Cl (24.2%) in CH_3Cl.

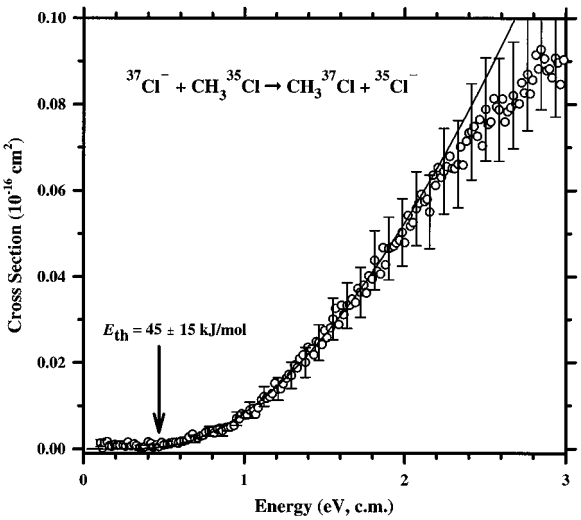

Figure 10. Cross section for the threshold region of reaction 3, $^{37}Cl^- + CH_3{}^{35}Cl \rightarrow {}^{35}Cl^- + CH_3{}^{37}Cl$, as a function of energy in the center-of-mass frame. The apparent cross section has been scaled to account for the fractional abundance of the $CH_3{}^{35}Cl$ isotopomer in the chloromethane reactant gas. The circles are experimental data from a single set of measurements using the pulsed ion beam mode with $\tau_1 = \tau_2 = 1.5$ ms. The solid line is the best fit of eq 12 with $E_{th} = 0.46$ eV (45 kJ/mol) and $N = 2.64$, convoluted over experimental energy distributions as described in the text.

2. Near-Thermal Energies. At energies below 0.4 eV, the cross section for reaction 3 is zero or extremely small. The presence of trapped ions (see section II. C.5) means that we can obtain only upper limits on the reaction cross sections at these low energies. Decreasing the ion pulse width lowers the

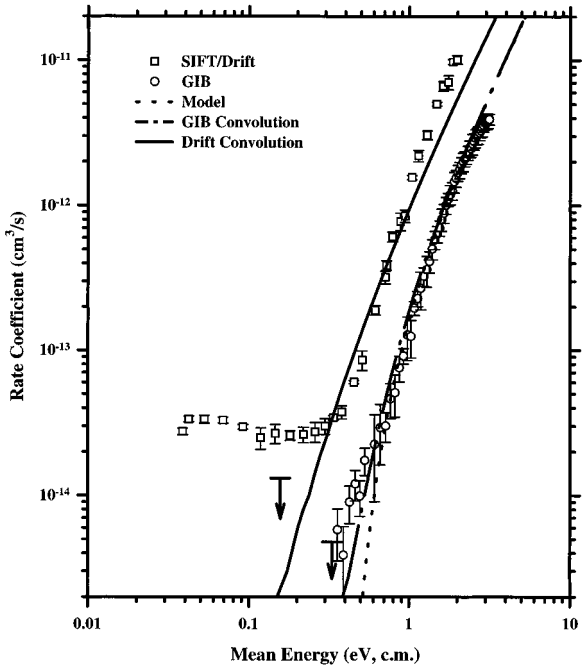

Figure 11. Comparison of cross section data with the SIFT/drift results of Bierbaum and co-workers.[7] The squares represent the drift tube rate coefficients as a function of the mean energy in the center-of-mass frame. The circles are the cross sections from the present work converted to rate coefficients as a described in the text. Arrows show upper limits of the rate coefficients from the present work using two different ion pulse widths ($\tau_1 = \tau_2 = 1.5$ ms at $\langle E\rangle_{min} = 0.16$ eV $\tau_1 = \tau_2 = 1.0$ ms at $\langle E\rangle_{min} = 0.34$ eV). The dashed line is the unconvoluted model cross section (eq 12) with the same parameters as shown in Figure 10, converted to a rate coefficient, and the dash−dot line is the model convoluted over the experimental energy distributions in the GIB experiments. The solid line is the model cross section convoluted over the drift tube ion energy distribution using the programs of Viehland and co-workers.[107]

apparent (false) cross section due to trapped ions, but it also raises the minimum collision energy that is accessible. We obtain upper limits of $\sigma \leq (9 \pm 3) \times 10^{-20}$ cm^2 at 0.14 eV c.m. (using $\tau_1 = \tau_2 = 1.5$ ms) and $\sigma \leq (4 \pm 3) \times 10^{-20}$ cm^2 at 0.32 eV c.m. ($\tau_1 = \tau_2 = 1.0$ ms). The higher upper limit at lower energy (longer pulses) results from residual trapped ion effects, not the intrinsic behavior of the cross section.

For comparison of our reaction cross section data with the measurements of $k(E)$ in SIFT/drift experiments by Bierbaum and co-workers,[7] we have converted[45] our cross sections to energy-dependent rate coefficients according to $k(\langle E\rangle) = \sigma(E_{cm})v_{rel}$, where $v_{rel} = (2E_{cm}/\mu)^{1/2}$ is the relative collision velocity, $\langle E\rangle = E_{cm} + (3/2)\gamma k_B T$ is the mean energy of the distribution, and $\gamma = M_{ion}/(M_{ion} + M_{gas})$. The comparison is presented in Figure 11. The raw rate coefficients disagree in two respects. First, the drift tube rate coefficient is approximately constant with $k = 3.5 \times 10^{-14}$ cm^3 s^{-1} from thermal energy (300 K or $\langle E\rangle = 0.039$ eV) up to 0.4 eV, while the present results give upper limits to the rate coefficient that are a factor of 2−6 times smaller from 0.1 to 0.3 eV. Second, the threshold feature rises more rapidly with a lower energy onset in the drift tube data than in the GIB data. The two experiments at our lowest-energy measurement ($\langle E\rangle = 0.16$ eV c.m.) are within the mutual uncertainty limits (±50% in absolute magnitudes for both experiments). However, our rate coefficients below 0.3 eV are only *upper limits* because of the residual effect of the trapped ion reactions. We believe eliminating the trapped ions entirely would lower the apparent cross sections at near thermal energies, thereby increasing the discrepancy between the flow tube and the GIB results. On the other hand, the present experiment is less well suited in principle for measuring *thermal* rates than is the flow tube method, and therefore further independent investigations would be desirable. Given the reaction efficiency of only 1 in 50 000 collisions, impurities or secondary reactions would tend to increase the apparent reaction probability in either experiment. Bierbaum and co-workers[7] carefully checked for the possibility of reactions with chlorine-containing impurities, however, and no evidence for impurities was discovered in the present work.

TABLE 2: Threshold Fits[a]

reaction	σ_0	N	E_{th} (eV)	fit type
(3) $^{37}Cl^- + CH_3{}^{35}Cl \rightarrow$ $^{35}Cl^- + CH_3{}^{37}Cl$	0.024	2.64	0.47 ± 0.16	full optimization
	0.016	3.00	0.34	fixed N
	0.026	2.50	0.50	fixed N
	0.043	2.00	0.70	fixed N
(5) $Cl^-\cdots CH_3Cl + Xe \rightarrow$ $Cl^- + CH_3Cl + Xe$	16.1	1.21	0.41 ± 0.12	full optimization
(13) $Cl^- + CH_3Cl \rightarrow$ $Cl_2^- + [CH_3]$	0.09	2.0	4.3 ± 0.4	full optimization

[a] Uncertainties represent the 2σ deviation in the threshold energies, estimated as described in the text.

Although other systematic errors in either experiment cannot be absolutely excluded, the deviation between the two experiments at low energies could also be a result of real differences in reaction conditions. Because the reaction rate is extremely small, temperature and pressure differences could have a large effect. In principle, the GIB beam/gas configuration yields a Maxwell−Boltzmann distribution with an effective temperature[45] of $T_{eff} = \gamma T = 125$ K for reaction 3 at zero ion beam energy, that is, a lower temperature than in the 300 K flow tube experiment at zero drift field. In practice, however, we cannot achieve such a low effective temperature. First, the pulsed ion beam mode of operation limits the collision energies to $\langle E\rangle >$ 0.16 eV c.m. or higher. Second, the effective temperature T_{eff} applies to the limit of zero ion velocity (stationary ions), but there is actually a finite ion energy spread even at the nominal zero beam energy. Because the S_N2 barrier could produce a strong temperature dependence for reaction 2, it would be worthwhile for experiments to be repeated as a function of temperature (our instrument is not currently capable of varying the gas cell temperature). Another difference in conditions between the flow tube and the GIB experiments is that the GIB experiments are rigorously in the single-collision limit (with the extrapolation to zero-pressure), while the flow tube experiments are carried out in 0.5 mbar of helium buffer gas. Possible mechanisms for a buffer gas collision effect will be considered in the Discussion.

3. Threshold Feature. *Empirical Threshold Law Fit.* The chloride exchange cross section for reaction 3 rises from an apparent threshold of about 0.5 eV (50 kJ/mol) and reaches an initial plateau of about 0.09×10^{-16} cm^2 at 4 eV. An empirical threshold law fit to the cross section data for reaction 3 using eq 12 with $P_D = 1$ is shown in Figure 10. Experimental[103] vibrational frequencies and rotational constants of CH_3Cl are used for the sum over reactant internal energies. The best fit to the data is obtained with $E_{th} = 0.47 \pm 0.16$ eV (45 ± 15 kJ/mol) and $N = 2.64$. Rather large uncertainty limits for this system are obtained because the threshold energy is sensitive to the energy range of the fit and the value of N. Reasonable fits to the data could be obtained for $N = 2-3$ (see Table 2). The threshold fits are fairly insensitive to the inclusion of internal energy in eq 12. The empirical translational energy threshold of 45 ± 15 kJ/mol is substantially higher than the reported barrier height[7−11] of 10−13 kJ/mol and all theoretical

TABLE 3: Enthalpies of High-Energy Reaction Channels[a]

$Cl^- + CH_3Cl$	0
$Cl_2^- + CH_3$	223 ± 19
$CHCl_2^- + H_2$	250 ± 17
$CH_2Cl^- + HCl$	262 ± 6
$Cl^-\cdots HCl + CH_2$	280 ± 10
$Cl^- + Cl + CH_3$	349 ± 2
$Cl + CH_3Cl + e^-$	349.0 ± 0.3
$Cl^- + HCl + CH_2$	380 ± 2
$CCl_2^- + H_2 + H$	517 ± 42
$Cl_2^- + CH + H_2$	672 ± 19
$Cl_2^- + CH_2 + H$	685 ± 19

[a] ΔH_{300} in kJ/mol.[113]

estimates (Table 1). That implies either that the translationally activated reaction goes by a different mechanism than S_N2, or that there is a dynamical impediment to the reaction (vide infra).

Comparison with Drift Tube Results. In comparison with the SIFT/drift results (Figure 11), the threshold feature for the GIB experiment rises at higher energies. This apparent discrepancy can be resolved by considering the different ion velocity distributions in the two experiments. At energies above 0.5 eV, the GIB distribution is approximately Gaussian with a narrow relative width,[98] $W_{1/2} \approx (11.1\gamma k_B T E_{cm})^{1/2}$ fwhm. The energy distribution in the drift tube is given to first order by a Maxwell−Boltzmann distribution with $T = \langle E \rangle / k_B$ but is significantly nonisotropic with respect to the electric field direction and has a non-Maxwellian high-energy tail.[104−107] The broader overall energy distribution in the drift tube and, especially, its high-energy tail accounts for the faster rise of the threshold feature in the drift tube data compared with the GIB results. We can quantify the comparison of the threshold feature between the GIB cross sections and the SIFT/drift rate coefficients by convoluting our model cross section over the actual drift tube ion energy distribution, using a calculated Cl^-−He interaction potential[108] and the on-line simulation program of Viehland and co-workers.[107] The input reaction cross section is the threshold law model (eq 12) with our best-fit parameters given in Table 2. The resulting calculated rate coefficient, $k(E)$, is shown in Figure 11. The match with the experimental results of Bierbaum and co-workers[7] is good in the onset region, which confirms that both experiments are measuring the same process. Bierbaum and co-workers[7] obtained a threshold energy of 2 eV, but they used a simple Maxwell velocity distribution for their deconvolution, which does not adequately reproduce the true energy distribution at high drift fields for processes with a steeply rising cross section.

Statistical Modeling. Chesnavich and Bowers[89] used transition-state theory to derive expressions for the threshold behavior of direct translationally driven reactions. Using the D_{3h} tight transition state for the S_N2 reaction, their result for the threshold cross section in the classical limit gives an expression identical with our empirical power law (eq 11) with $N = 2$. Fits using $N = 2$ yield $E_{th} = 67$ kJ/mol (Table 2), significantly higher than the fully optimized empirical threshold. The translationally driven transition-state theory pertains to direct reactions and may not be valid if the formation of a $Cl^-\cdots CH_3Cl$ intermediate complex is important.

We have also modeled the threshold behavior using classical phase space theory (PST),[88,109−112] the variant of transition-state theory that rigorously conserves angular momentum. Following the PST calculation of Graul and Bowers,[11] we employ a loose transition state at the centrifugal barrier for the entrance channel and a tight transition state corresponding to the D_{3h} configuration for the S_N2 reaction. The molecular parameters for reaction 2 were taken directly from Table 3 of Graul and Bowers,[11] except that the barrier height was varied and the absolute magnitude was scaled for comparison with experiment. Using the barrier height found by Graul and Bowers[11] to match the thermal rate, $E_B(0\ K) = 12$ kJ/mol, yields a cross-section excitation function that rises much too rapidly at low energies compared with the experimental threshold behavior. The best fit of the data is obtained with $E_B(0\ K) \approx 0.43$ eV or 41 kJ/mol, but scaling the magnitude down by a factor of 3.0 is required to match the experiment, which is outside the estimated ±50% experimental uncertainty.

The implementation of PST[88,109−112] used here treats all nonlinear molecules as spherical tops, which simplifies the integrations over the available phase space volume. The D_{3h} transition state for the S_N2 process (Figure 2) is actually extremely prolate. We found that the PST threshold behavior and magnitude of the cross section is sensitive to the value of the (spherical) rotational constant used for the transition state. Therefore, the PST model used here may not be very accurate for this system, particularly at elevated translational energy, which generates high orbital angular momenta in the collision complex. A calculation of the PST cross section without simplifying approximations would be useful. The threshold energy found using PST is slightly lower than the best fit of the empirical model (~41 mol versus 45 kJ/mol, respectively). Although these agree well within the mutual uncertainties, the lower value from PST would imply that angular momentum constraints may be important for the S_N2 reaction.

4. High-Energy Reaction Channels. Diatomic chlorine anion products are formed at high energies with an energy threshold of $E_{th} = 410 \pm 40$ kJ/mol, corresponding to reaction 13:

$$Cl^- + CH_3Cl \rightarrow Cl_2^- + [CH_3] \qquad (13)$$

as shown in Figure 9. The threshold energy for reaction 13 is much higher than the thermodynamic reaction enthalpy[113] of $\Delta_{13}H = 223$ kJ/mol (Table 3). The second, high-energy threshold for atomic chlorine anion at about 550 kJ/mol (Figure 9) roughly coincides with the peak in the cross section for reaction 13, and is probably due to the further decomposition of the Cl_2^- products:

$$Cl^- + CH_3Cl \rightarrow Cl^- + Cl + [CH_3] \qquad (14)$$

However, that second threshold feature is also well above the thermochemical enthalpy of reaction, $\Delta_{14}H = 349 \pm 2$ kJ/mol (Table 3). Collisional electron detachment[31] could also occur above 349 kJ/mol [EA(Cl) = 3.62 eV] but would not be detected in our experiments.

B. Kinetic Isotope Effect. Figure 12 compares the chloride exchange cross sections for CH_3Cl and CD_3Cl, (reactions 3 and 4). The deuterated chloromethane (Cambridge Isotope Laboratories, 98% deuterated) was used without further purification. Measurements of the kinetic isotope effect were made on the same day under identical experimental conditions at a single low gas cell pressure. Results on four different occasions were similar to Figure 12a, which shows the average of the best two data sets. Reactions 3 and 4 exhibit identical reaction energy thresholds within experimental uncertainty. Estimated vibrational zero-point energy differences between reactions 3 and 4 yield a barrier height difference that favors the deuterated system by only 0.07 kJ/mol, which is too small to influence the present results. The magnitude for the CH_3Cl cross section is about 20% higher than for CD_3Cl. As shown in Figure 12b, the kinetic isotope effect ratio, $\sigma_H/\sigma_D \approx 1.2 \pm 0.1$, is roughly constant from the threshold up to 4.5 eV.

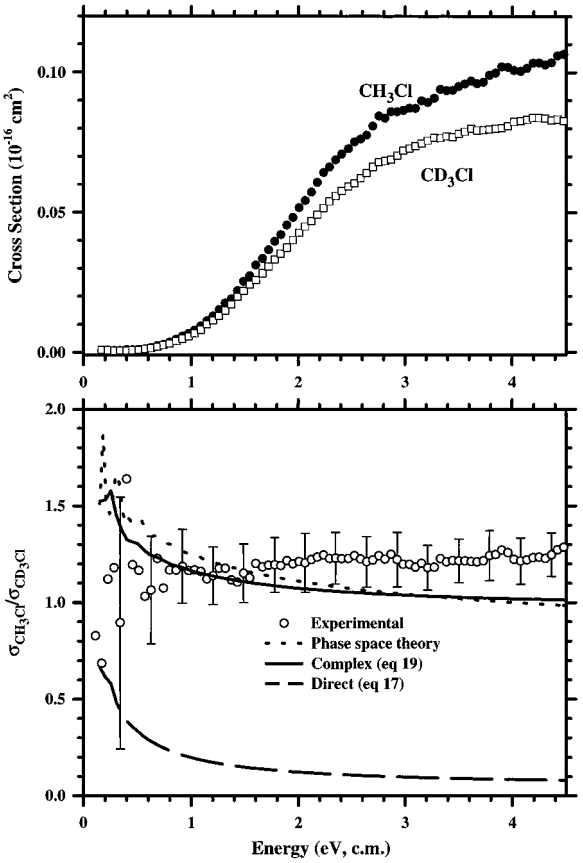

Figure 12. Kinetic isotope effect for the S_N2 chloride exchange reaction. Top: the solid symbols show the cross section for reaction 3, $^{37}Cl^- + CH_3{}^{35}Cl \rightarrow {}^{35}Cl^- + CH_3{}^{37}Cl$, and the open symbols show the cross section for reaction 4 $^{37}Cl^- + CD_3{}^{35}Cl \rightarrow {}^{35}Cl^- + CD_3{}^{37}Cl$. Both cross sections were measured at a single chloromethane pressure of about 0.1 μbar in the gas cell under nearly identical experimental conditions. Bottom: kinetic isotope effect ratio, σ_H/σ_D. Circles are the experimental values. Lines represent the models indicated in the legend and described in the text.

C. Collision-Induced Dissociation of the $Cl^-\cdots CH_3Cl$ Complex. The cross section for the collision-induced dissociation of $Cl^-\cdots CH_3Cl$ complexes with xenon target gas (reaction 5) as a function of collision energy is shown in Figure 13. The complexes are formed by the association of chloromethane with chloride ions in the flow tube source. The CID data represent the linear extrapolation of three scans at different Xe pressures to zero pressure. Exothermic formation of $Cl^-\cdots H_2O$ by ligand exchange from background water in the octopole chamber or water impurity in the xenon gas was also observed at low energies but did not interfere with the CID cross-section measurement.

The CID cross section threshold is fit with eq 12 as described above. For the RRKM model of the dissociation probability, we use vibrational frequencies and rotational constants for the C_{3v} complex taken from ab initio calculations[114] at the HF/6-31G(d) level (vibrational frequencies scaled[115] by 0.89). The best fit is shown in Figure 13, with threshold energy $E_{th} = 0.41 \pm 0.12$ eV or 39 ± 12 kJ/mol. There is no appreciable kinetic shift for this system; the loose and tight transition-state limits[93] give identical results. The correction from the 0 K threshold energy value to the complexation enthalpy at 300 K is only -0.3 kJ/mol, giving $\Delta_C H_{300K} = 39 \pm 12$ kJ/mol, where we have calculated integrated heat capacities using the ab initio molecular constants.

The threshold energy for CID of $Cl^-\cdots CH_3Cl$ provides an independent measure of the well depth of the ion−dipole

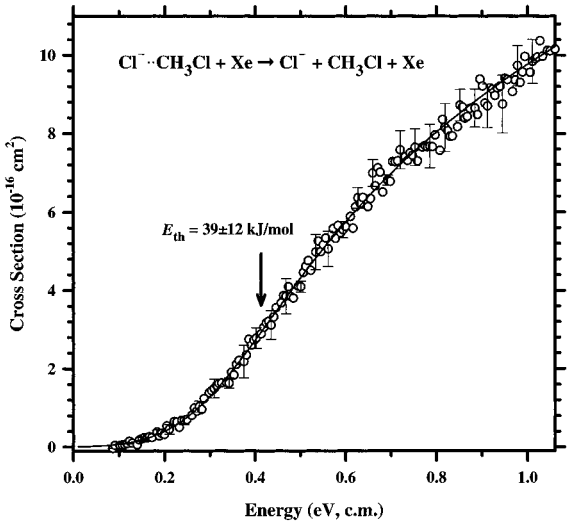

Figure 13. Collision-induced dissociation cross section of $^{35}Cl^-\cdots CH_3{}^{35}Cl$, reaction 5, as a function of collision energy in the center-of-mass frame. The circles show the experimental data, and the solid line is a convoluted fit of eq 12 to the data with $E_{th} = 0.41$ eV and $N = 1.2$

complex. Our value agrees with the more precise recent high-pressure mass spectrometer equilibrium measurement[40] of $\Delta_C H_{300K} = 43.5$ kJ/mol (10.4 kcal/mol) within experimental uncertainty. This agreement implies that the flow tube source produces a thermalized distribution of complex ions. Ab initio values of the well-depth, given in Table 1, are also in good agreement with the experimental values.

IV. Discussion

A. Low-Energy Behavior. At energies below the apparent threshold our measured cross sections for reaction 3 are small, at or below our detection limits for $E_{cm} < 0.3$ eV, and the corresponding reaction rate coefficients are smaller than those obtained by Bierbaum and co-workers[7] at low energies. Our GIB results are strictly in the zero-pressure single-collision limit, while the drift tube reactions are carried out with a helium buffer gas pressure of about 0.5 mbar. The lifetime of the $Cl^-\cdots CH_3Cl$ collision complex is estimated from HPMS measurements[40] to be 12−27 ps at 300 K, and its Langevin collision frequency with He at the drift tube pressure is about 6.5×10^6 s^{-1}. Thus, one in every 5700−13000 complexes formed undergoes a collision with helium during its lifetime. The reported thermal rate coefficient[7] corresponds to only one reaction per 50 000 complex-formation collisions, which means that the reaction rate corresponds to $^1/_4$ to $^1/_9$ of the complexes that have collided with helium. Therefore, collisions could possibly be important in inducing the exchange reaction at the flow tube pressure. Even grazing collisions of the $Cl^-\cdots CH_3Cl$ complex might be sufficient to redistribute its energy and angular momentum and allow exploration of more of the phase space volume, including the constricted transition state region leading to the exchange reaction. If a collision stabilizes the $Cl^-\cdots CH_3Cl$ complex, then it can no longer react or decompose back to reactants, but further collisions could reactivate it. Our ability to make thermal $Cl^-\cdots CH_3Cl$ complexes in our flow tube ion source implies that collisional stabilization of the complexes can be important at pressures similar to those used by Bierbaum and co-workers.[7] If collisions are important, there would be a strong dependence of the measured bimolecular thermal rate coefficient on the buffer gas pressure in flow tube experiments. The pressure dependence has not been measured for reaction 2.

For the exothermic reaction $Cl^- + CH_3Br \rightarrow Br^- + CH_3Cl$, Grimsrud and co-workers[116,117] found an enhancement of the

effective bimolecular rate coefficient for S_N2 by a factor of 4 for an increase in the pressure from 0.005 to 0.85 bar at 398 K. Collisional stabilization of the $Cl^-\cdots CH_3Br$ intermediate is believed to be responsible because for that case the S_N2 barrier is slightly lower than the energy of reactants. No pressure dependence over the same range was found for the $Cl^- + RBr$ (R = ethyl or *n*-butyl) S_N2 reactions, possibly because these have long-lived complexes and are therefore already in the high-pressure limit at lower pressures.[117] Collisional stabilization and establishment of a thermal distribution of the complex in the present case would tend to favor decomposition back to reactants instead of formation of S_N2 products, but the latter might also occur. Formation of a relatively long-lived complex might also promote reaction via tunneling, as suggested for the exothermic $Cl^- + CH_3Br$ S_N2 reaction.[118] Grimsrud and co-workers[119] observed $Cl^-\cdots i\text{-PrBr} \rightarrow Br^- + i\text{-PrCl}$ (*i*-Pr = isopropyl), for which the S_N2 barrier is slightly above that of reactants such as in reaction 2, for thermalized complexes. The central barrier is lower for the $Cl^- + i$-PrBr case (6.7 vs 10−13 kJ/mol for reaction 2), but the transition state has more steric hindrance.

B. Threshold Process. Bierbaum and co-workers[7] attributed the higher-energy threshold process observed in the drift tube experiments to front-side anionic attack by Cl^- on CH_3Cl. We believe that our threshold process and the feature observed in the drift tube study are the same, but that the mechanism is actually translationally activated S_N2 nucleophilic displacement by conventional back-side attack. Our arguments follow.

The drift tube rate coefficients and our GIB cross sections rise from the same threshold energy, after taking into account the energy distributions of the two experiments. The excellent match in the onset region between the drift tube data and the model threshold law fit to our data and then convoluted over the drift tube energy distributions (Figure 11) demonstrates that the two observed features are the same. The threshold energy is 45 ± 15 kJ/mol based on the fit of the empirical threshold law (eq 12) or ∼41 kJ/mol based on the phase space theory model. The major source of our uncertainty is from modeling the threshold dependence of the reaction.

Consistent with their estimate of a threshold of 190 kJ/mol, Bierbaum and co-workers[7] proposed that the mechanism of the process was anionic attack on the chlorine side of chloromethane. Subsequent theoretical studies by Ziegler and co-workers[28] and Radom and co-workers[27] lent credence to such a mechanism. They found a high-lying saddle point (one imaginary frequency) for $CH_3Cl_2^-$ in C_s symmetry, distinct from the D_{3h} transition state for the S_N2 nucleophilic displacement mechanism (compared in Figure 2). At the G2(+) level,[27] the energy of the C_s saddle point is 194 kJ/mol above the reactants, in close agreement with the originally reported drift tube threshold energy. Radom and co-workers[27] pointed out that the C_s saddle point actually corresponds to front side nucleophilic attack at the carbon and not halophilic or anionic attack at the chlorine atom in chloromethane. Halophilic attack is still higher in energy, and no minimum was found for front-side approach of Cl^- at the chlorine atom in CH_3Cl along the C_{3v} axis.[27] Although the C_s saddle point energy is very near the (overestimated) threshold of 190 kJ/mol reported by Bierbaum and co-workers,[7] that is simply a misleading coincidence. The calculated energies for the C_s transition state are too high for it to be involved in the reaction mechanism near our observed threshold energy of 45 ± 15 kJ/mol.

If anionic or front-side attack via that saddle point is not possible at the threshold energy, then is the actual mechanism S_N2 or some other process? Table 3 compiles the thermochemical threshold energies for other asymptotic reaction channels. Each channel, besides chloride exchange, is much too high to be involved directly in the exchange reaction at threshold, even considering an additional stabilization by formation of the corresponding ion−neutral complex. To illustrate possible reaction pathways, we have calculated energies at the HF/6-31G(d) level[114] for several cuts through the global potential energy surface for $CH_3Cl_2^-$, presented in Figures 14 and 15. Figure 14 shows energies for $CH_3Cl_2^-$ configurations with identical chlorine atoms, but with varying Cl−C−Cl angles. For each point in Figure 14, the Cl−C−Cl angle is fixed and the two C−Cl bond lengths are held equal, but the bond lengths and the positions of the hydrogen atoms are optimized within the overall symmetry. The two C_{2v} geometries (Figure 2) correlate with the D_{3h} S_N2 transition state but with the Cl−C−Cl angle bent symmetrically away from 180°. The C_s symmetries are related to the higher-energy saddle point. For the C_{2v} configurations, the energy rises rapidly from the minimum at 180°, corresponding with the restricted cone of acceptance for back-side S_N2 attack by Cl^- on CH_3Cl. The C_s configurations have a minimum energy at the $CH_3Cl_2^-$ transition state at a Cl−C−Cl bond angle of 95° and C−Cl bond lengths of 2.72 Å at the HF/6-31G(d) level (85° and 2.41 Å, respectively, at the MP2/6-31G(d,p) level[28]). The energies rise rapidly for smaller angles. For larger angles, the energy changes little but is accompanied by rapid extensions of the two C−Cl bond lengths. Figure 15 is an alternate representation showing the potential energy surface as a function of the distance and angle

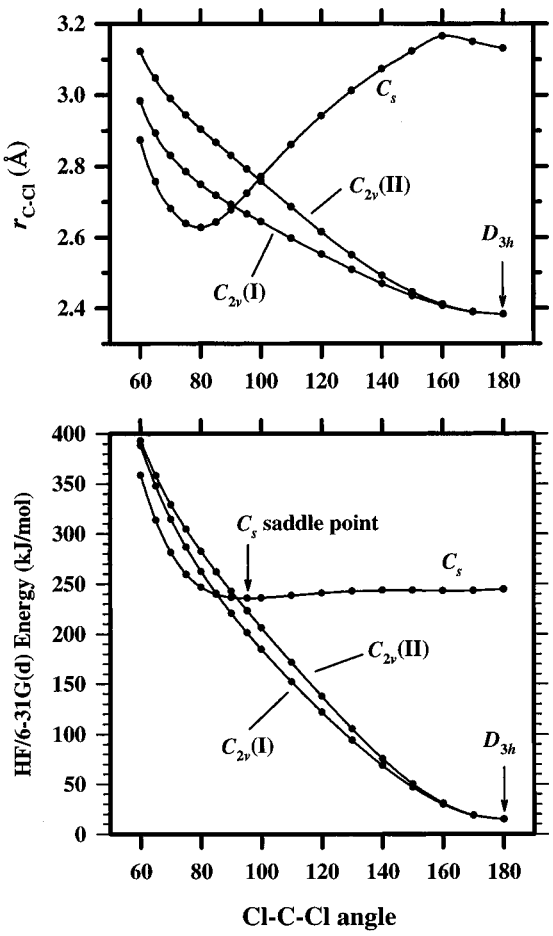

Figure 14. Energies of $CH_3Cl_2^-$ relative to $Cl^- + CH_3Cl$ as a function of the Cl−C−Cl bond angle for three symmetries (shown in Figure 2) with identical chlorine atoms, at the HF/6-31G(d) level of theory (lower plot). At each point, all bond lengths and bond angles are optimized except the Cl−C−Cl angle is fixed and the two C−Cl bond lengths (upper plot) are held equal.

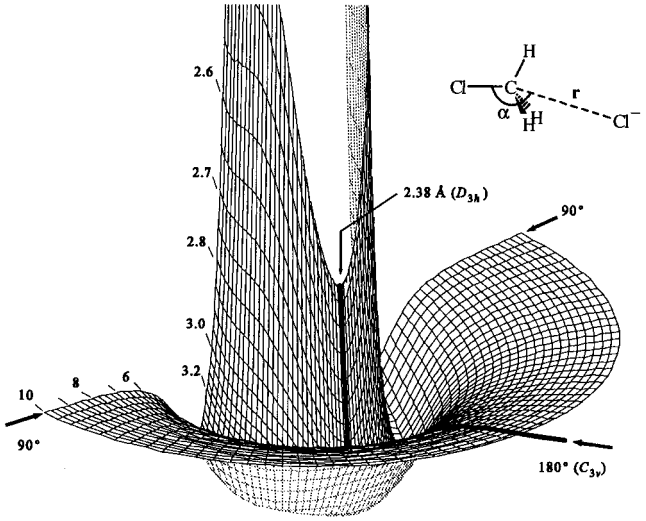

Figure 15. Potential energy surface for approach of Cl^- to CH_3Cl as a function of the C−Cl distance (radius from the origin in the horizontal plane, in angstroms) and the Cl−C−Cl bond angle (polar angle). The mesh points in the vertical direction are calculated HF/6-31G(d) energies with all other geometric parameters fully optimized (including rotations of the methyl group). The dark solid line corresponds to the minimum energy path in C_{3v} symmetry, which is also shown in Figure 1, that leads to the S_N2 transition state at the D_{3h} saddle point. The inner rim extending upward from the saddle point represents the point where the bond length of the leaving Cl atom is equal to that of the incoming Cl atom.

of approach of the choride anion, with all other bond lengths and angles fully optimized. It shows that the deep well of the ion−dipole complex is fairly isotropic for Cl−C−Cl angles from 180° (C_{3v} approach) to 90°, but that the opening over the S_N2 barrier crossing is a narrow notch on the steep inner repulsive wall.

The C_s saddle point for front-side attack can be definitively excluded near the observed threshold based on its high energy. Nevertheless, it is interesting to examine the relationship between the C_{2v} and C_s configurations at Cl−C−Cl angles near 90°, that is, near the higher-energy saddle point. At the HF/6-31G(d) level, the energy of two C_{2v} configurations are *lower* than the C_s configuration at this angle, and the C−Cl bond lengths are similar (Figure 14). Transformation to the lower-energy symmetry, C_{2v} (I) in Figure 2, requires only a rotation of the methyl group and a reduction of the C−Cl bond length from 2.72 to 2.67 Å. Thus, although the C_s geometry has the distinction of having a true saddle point on the potential energy surface, it is actually only a narrow ridge or shelf on the inner repulsive wall above the deep valley of the ion−dipole complex (Figure 15). The intrinsic reaction path (IRP) calculations by Ziegler and co-workers[28] show a quite convoluted path from the alternative transition state down to the ion−dipole complex, and similarly Glukhovtsev et al.[27] find that the IRP for both front-side and back-side attack involve the same C_{3v} ion−molecule complex. On the basis of our HF/6-31G(d) calculations,[114] the system must pass over a high barrier (>380 kJ/mol) to reach the C_s saddle point via Cl^- approach along a fixed Cl−C−Cl angle of around 95°. This corresponds to the inner repulsive wall in Figure 15. The C_s saddle point is unlikely to be important in the exchange reaction at any energy because it corresponds to a restricted region of phase space that is contiguous to the lower-energy back-side attack region.

Another possible mechanism that might be considered for the threshold process involves the charge transfer state of reactants, $Cl + [CH_3Cl]^-$. In the asymptotic region, the charge-transfer state is calculated at the multireference MP2 level[120]

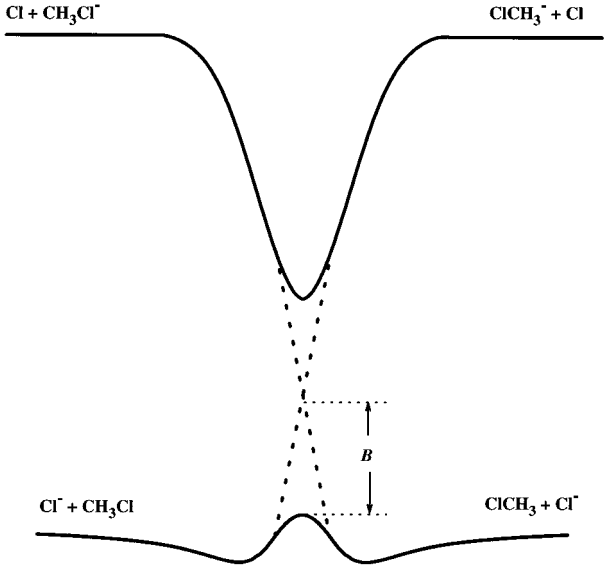

Figure 16. Schematic energy diagram showing the avoided crossing between $Cl^- + CH_3Cl$ reactants and the $Cl + CH_3Cl^-$ charge-transfer state. The energies of the upper state are poorly characterized.

to lie 600 kJ/mol above $Cl^- + CH_3Cl$, much too high to be involved directly in the observed threshold process. At close range, the S_N2 transition-state barrier arises from an avoided crossing between the reactants and the charge-transfer state,[1,19,121,122] shown schematically in Figure 16. The potential energy maximum on the ground electronic surface produced by the avoided crossing at the S_N2 barrier has a corresponding minimum on the upper electronic surface. One could imagine a nonadiabatic electronic transition to the upper surface, induced by the collision, followed by a transition back to the lower surface with loss of distinction between the two chlorine atoms. Both nonadiabatic transitions would have low probability, but the mechanism is possible in principle and would result in a small chloride-exchange cross section. The question is whether the energy gap between the two surfaces is small enough for transitions to be allowed at the observed threshold energy of 45 ± 15 kJ/mol. Shaik and co-workers[19] estimated the gap between the diabatic crossing point and the lower surface (B in Figure 16) to be 60 kJ/mol (14 kcal/mol) for the halide/halomethane S_N2 reactions in general, but their recent calculations[1] for $F^- + CH_3F$ give $B \approx 110$ kJ/mol. The gap between the two adiabatic surfaces would be about $2B$, giving a minimum transition energy of $E_B + 2B \approx 130$ kJ/mol using the lower value, which is still too high for it to be involved at our observed threshold. Malrieu and co-workers[120] calculate that the diabatic potential energy curves cross at an energy of 210 kJ/mol above the entrance channel, much larger than the previous estimates. Such a high crossing point implies that the upper adiabatic surface cannot be implicated in the mechanism for the present observed reaction near threshold.

Eliminating these other possibilities leaves us to conclude that the translationally activated exchange near threshold occurs by the conventional S_N2 back-side attack mechanism, with inversion of the carbon center. At the HF/6-31G(d) level (Figure 14), only the C_{2v} geometries with Cl−C−Cl bond angles larger than about 150° are accessible at the observed threshold energy of 45 ± 15 kJ/mol. Therefore, *the observed exchange reaction occurs by passage over the true S_N2 transition state for back-side attack,* at least near threshold.

The experimental threshold energy of 45 ± 15 kJ/mol is substantially higher than the S_N2 barrier height of 10−13 kJ/mol supported by the thermal rate measurements and ab initio

calculations (Table 1). How reliable is the latter value for the true barrier height? The reported thermal rate coefficient[7] of $k = (3.5 \pm 1.8) \times 10^{-14}$ cm^3 s^{-1} at 300 K is near the lower limit of the SIFT/drift method and could not be verified by the present experiments (as discussed above). The extraction of a barrier height from the thermal rate depends on statistical transition-state theory modeling[8−11] of a reaction that is nonstatistical according to classical trajectory calculations.[15,16] Furthermore, other calculations of the 300 K rate coefficient vary substantially from the experimental value.[7] Okuno[123] obtains $k = 6.41 \times 10^{-15}$ cm^3 s^{-1} using transition-state theory with a barrier height of $E_B = 11.7$ kJ/mol (2.80 kcal/mol). The quantum scattering calculations by Clary and Palma[30] indicate that the reaction probability is very sensitive to the length of the C−Cl bond at the transition state on the potential energy surface, which in turn is quite sensitive to the level of theory in ab initio calculations. They obtain $k = 2.5 \times 10^{-15}$ cm^3 s^{-1} or 1.3×10^{-14} cm^3 s^{-1} on potential energy surfaces both with $E_B = 15$ kJ/mol (3.6 kcal/mol) but with slightly different C−Cl bond lengths in the transition state, $r = 2.38$ or 2.30 Å, respectively. The ab initio calculations of the barrier height (Table 1) also are highly dependent on the size of the basis set and the level of electron correlation. The presence of the avoided surface crossing (Figure 16) may complicate the theoretical calculations. Nevertheless, the correspondence between the experimental barrier height and high-level theory leaves little likelihood that the true barrier height could be as high as our empirical threshold energy of 45 ± 15 kJ/mol. Therefore, despite these caveats, it is most probable that the actual S_N2 barrier height is around 10−13 kJ/mol.

There are several factors that could reasonably account for a translational energy of activation in excess of the minimum potential barrier. The classical trajectory calculations by Hase and co-workers[14] show that translational energy is ineffective at promoting the S_N2 reaction. Reasons for that are the constricted geometry of the transition state, requiring direct attack along the C_{3v} axis to pass over the barrier at low energies, the difficulty of converting translational energy into the internal C−Cl stretch of CH_3Cl that is required to reach the transition state, and angular momentum constraints. Rotation of the chloromethane neutral reactant also impedes reaction according to the trajectory calculations.[14] If the reaction is very inefficient at energies just above the barrier due to dynamical constrictions, then our observed threshold probably does not represent an energy where a new mechanism suddenly turns on, but rather the sensitivity threshold of the experiment.

Classical trajectory calculations by Hase and co-workers[14] indicate that increasing the translational energy is "unimportant" in promoting the substitution reaction (1, 0, 1, and 3 substitution events in 200 trajectories at $E = 21$, 42, 63, and 105 kJ/mol, respectively, at zero impact parameter, $T_{rot} = 0$ K, and with vibrational zero-point energy added). That is generally consistent with our elevated translational threshold, but the calculated cross sections do not agree with the experiment. At $E = 209$ kJ/mol (2.17 eV), a cross section of $(0.28 \pm 0.09) \times 10^{-16}$ cm^2 was calculated (four substitutions in 300 trajectories with the same conditions except random impact parameters), which is over 5 times larger than the experimental cross section. On the basis of trajectories at thermal energies,[14] inclusion of CH_3-Cl rotational energy would likely decrease the calculated cross section and bring it into better agreement with experiment. Semiclassical reaction path dynamics calculations[29] yielded cross sections over 0.3×10^{-16} cm^2 for several product vibrational states at a total reaction energy of 50 kJ/mol (0.5 eV), which is also much larger than experiment. The cross section threshold behavior is likely to be very sensitive to the shape of the potential energy surfaces, and therefore further exploration and comparison with our new experimental results with dynamics calculations would be valuable.

Several mechanisms can be hypothesized to explain the observed onset of the translationally activated S_N2 reaction in the vicinity of 30−60 kJ/mol. First, at energies well above the S_N2 saddle point, the geometric constrictions may simply open up enough to allow reaction at an observable rate. Figures 14 and 15 show that the tight angular constriction of the D_{3h} transition state opens up to some extent at higher energies. Higher energies also reduce the influence of the ion−dipole well and the possibility of trapping trajectories in motion of the complex. A crude estimate of the geometry effect can be found by calculating an energy-dependent steric reaction probability:[91,92]

$$P(E-E_B) = (1/4\pi) \int_0^{2\pi} d\phi \int_0^{\theta_{max}(E-E_B)} \sin(\theta)\, d\theta \qquad (15)$$

where $\theta_{max}(E-E_B)$ is the maximum angle of the Cl^- approach away from collinear Cl−C−Cl (defined as $\theta = 0$) as a function of energy above the S_N2 barrier and ϕ is the azimuthal angle (neglecting any torsional potential). Equation 15 calculates the fractional solid angle of the cone of acceptance for approaches of Cl^- deviating directly along the C_{3v} minimum energy path. Taking the maximum angle from the HF/6-31G(d) calculations [by inverting the C_{2v}(I) curve in Figure 14], we calculate steric factors $P(E-E_B)$ of 0.0095, 0.018, 0.040, 0.061, 0.085, and 0.105 for energies above the barrier of 5, 10, 20, 30, 40, and 50 kJ/mol, respectively. The small steric factors near threshold would effectively slow the rise in the cross section and shift the apparent threshold to higher energies. The magnitude of the shift is difficult to quantify because it would depend on the energy dependence of the cross section apart from the steric factor (a line-of-centers model with eq 15 yields simply eq 11 with $N = 2$ near threshold)[91,92] and on the instrumental sensitivity. Qualitatively, these estimated steric factors can partially account for the small magnitudes of the cross sections for reaction 3 relative to a hard-sphere cross section.

A second possible mechanism involves translational-to-vibrational (T−V) energy transfer. In the trajectory calculations,[14] the CH_3 deformation mode was ineffective in promoting the substitution reaction but strong enhancement of the reaction was observed with three or more quanta in the C−Cl stretch mode. Three quanta of C−Cl stretch add 28 kJ/mol of vibrational energy. Adding that vibrational energy to the reported barrier height would yield an effective barrier of 38−41 kJ/mol, near the observed threshold energy. If T−V energy transfer itself is inefficient, then the effective threshold could be still higher. Exothermic variants of reaction 1 show no change in reactivity upon internal excitation of the halomethane reactant,[124] but that is unlikely to hold for reaction 2 because of its overall energy barrier.

Third, angular momentum constraints could explain a translational threshold energy above the true barrier height. High orbital angular momenta are generated by collisions at high translational energy. The angular momentum must be conserved as the system passes through the transition-state region. Because the moment of inertia of the tight transition state is much smaller than that of colliding reactants, high rotational energies are required to keep the same total value of angular momentum, which reduces the energy available along the reaction coordinate. Further constraints are necessary to account for the angular momentum of chloromethane. The classical phase space theory

model discussed above yielded a slightly slower onset to the reaction than the empirical threshold law fit, and therefore gave a lower threshold value (~41 versus 45 kJ/mol). A more sophisticated PST treatment would be needed to clarify the full effect of angular momentum constraints within statistical models. Still, it seems unlikely that PST or other statistical models could match the observed threshold behavior *while* also using the accepted barrier height of 10−13 kJ/mol. If the latter value is close to the true barrier height, as seems reasonable, then the translational activation of reaction 2 is decidedly nonstatistical. Further theoretical work is needed to unravel the details of the mechanism for translational activation.

C. Kinetic Isotope Effect. We investigated the kinetic isotope effect (KIE) for reaction 2 in the hope that it would provide some insight into the reaction mechanism. The observed kinetic isotope effect is "normal", $k_H/k_D > 1$, contrary to the "inverse" kinetic isotope effect predicted by transition-state theory[9,33−35] for reaction 2 at 300 K, $k_H/k_D = 0.96$, and observed[36−38,125] for exothermic variants of reaction 1, $k_H/k_D = 0.75-0.84$. The KIE has not been predicted for hyperthermal energies. Here we apply simple models to help determine what mechanisms might produce the observed isotope effect $\sigma_H/\sigma_D \approx 1.2$ in the threshold region for reaction 2.

The translationally driven transition state theory of Chesnavich and Bowers[89] yields a reaction cross section given by

$$\sigma(E) = h^2 W^{\ddagger}(E - E_B)/8\pi\mu E \qquad (16)$$

where $W^{\ddagger}$ is the sum of states at the transition state configuration, E is the translational collision energy, E_B is the barrier height (0 K), and μ is the reduced mass of reactants. This yields a KIE ratio given by

$$\sigma_H/\sigma_D = \mu_D W^{\ddagger}{}_H(E - E_B)/\mu_H W^{\ddagger}{}_D(E - E_B) \qquad (17)$$

We have calculated this ratio using the Beyer−Swinehart algorithm[95−97] for the sums of states with molecular constants for the D_{3h} transition state calculated[114] at the HF/6-31G(d) level (vibrational frequencies scaled by 0.89[115]) and $E_B(0\ K) = 13$ kJ/mol. This direct reaction model gives small KIE ratios, which does not match the experiment as shown in Figure 12.

Instead of a direct translationally driven reaction model, we can consider complex formation followed by statistical decomposition back to reactants or passage over the S_N2 transition state. For this mechanism, we obtain the following expression for the cross section:[126,127]

$$\sigma(E) = \sigma_c \frac{W^{\ddagger}(E - E_B)}{W^{\ddagger}(E - E_B) + 2W^R(E)} \qquad (18)$$

where σ_c is the complex formation cross section and W^R is the sum of states at the centrifugal barrier in the reactant channel. The KIE ratio is therefore given by

$$\frac{\sigma_H}{\sigma_D} = \frac{W^{\ddagger}{}_H(E - E_B)[W^{\ddagger}{}_D(E - E_B) + 2W^R_D(E)]}{W^{\ddagger}{}_D(E - E_B)[W^{\ddagger}{}_H(E - E_B) + 2W^R_H(E)]} \qquad (19)$$

The factors of 2 reflect the possibility of back-reaction after passage to the identical ion−dipole complex in the product channel; however, this is unimportant because $W^R \gg W^{\ddagger}$. The sums of states were calculated for $J = 0$, which implies W^R corresponds to free reactants (zero centrifugal barrier). The complex model is compared with the experimental ratio in Figure 12; it is a better match than the direct model, but unlike the data the calculated ratio decreases with increasing energy.

Because angular momentum constraints are likely to be important, we also calculated the KIE ratio using the PST model described above. The results (Figure 12) are similar to those of the complex model, and the energy dependence also does not match experiment. PST and the simple complex model do give the correct magnitude for the KIE from the threshold up to 1.5 eV c.m. That does not necessarily mean that a "long-lived" complex is formed that decomposes statistically. Rather, the models may simply reflect the relative large volume of phase space of the reactants versus the constricted phase space at the S_N2 barrier. The small volume of phase space for going over the barrier results in a low reaction probability for random collision events; the probability of a successful trajectory for a direct substitution might scale with the density of states calculated for the two isotopomers.

Another possible explanation for the KIE is quantum mechanical tunneling. Significant tunneling corrections were reported for reaction 2 in transition-state theory calculations by Tucker and Truhlar.[9] For a simple barrier crossing, tunneling is most important at low energies near the barrier. The observed KIE shows little energy dependence, however. For reaction 2, the barrier region is still constricted at energies above the barrier; therefore, tunneling might allow the reaction to cut corners on the potential energy surface, not just cut through the top of the barrier. A detailed consideration of tunneling is beyond the scope of this paper.

The $Cl^- + CH_3Br$ (CD_3Br) S_N2 reaction, which is exothermic with the central barrier below the energy of reactants,[128] exhibits an inverse kinetic isotope effect,[36−38,125] $k_H < k_D$, opposite the effect found for reaction 2. This difference between the two systems might be understood in terms of competition between decomposition of the initial complex back to reactants versus going over the barrier. For reaction 2, the energy of the barrier is higher than that of reactants, so the increase in density of states upon deuteration is greater for reactants than at the transition state. The reverse would be true for the $Cl^- + CH_3Br$ reaction.

D. High-Energy Abstraction. Endoergic formation of dihalide products, reaction 13 shown in Figure 9, occurs at high energies, well above the thermochemical threshold. Dihalide products have previously been reported for $Cl^- + CH_3Br$ and $Cl^- + CH_3I$ at hyperthermal energies.[129] For $Cl^- + CH_3Br$, an apparent threshold of ~200 kJ/mol was reported, just above the endoergicity of 170 kJ/mol. The authors[129] interpreted the process as attack at the halogen atom in a collinear arrangement rather than as front-side nucleophilic attack on carbon. Abstraction processes with energy thresholds much above the thermochemical threshold, as in the present case, are often associated with impulsive or stripping reaction mechanisms on a repulsive potential energy surface. At the apparent threshold of 410 ± 40 kJ/mol for reaction 13, the reactants can probably pass over the barrier for front-side attack. The peak of the cross section for reaction 13 correlates with the onset of decomposition to $Cl^- + Cl$ and the higher-energy feature in the Cl^- cross section.

V. Summary and Conclusions

We have measured the reaction cross section for the symmetric S_N2 exchange reaction between chloride anion and chloromethane as a function of collision energy using a new guided ion beam tandem mass spectrometer. The observed threshold energy is 45 ± 15 kJ/mol, which is an upper limit for the height of the S_N2 barrier on the potential energy surface. The error limits are primarily due to uncertainties in the theoretical methods for modeling the threshold behavior. An energy threshold of 30−60 kJ/mol is much higher than the

reported height of the potential energy barrier of 10−13 kJ/mol along the minimum energy path for S_N2 exchange. However, a previously proposed[7,27,28] mechanism involving front-side attack at the chlorine atom on chloromethane would require a much larger energy and can therefore be excluded near threshold. The excess barrier for translational activation of the S_N2 reaction is likely due to dynamical constraints, possibly including the restricted geometry of approach for passing over the barrier at low energies, angular momentum conservation at the tight transition state, and the difficulty of energy transfer between translational motion and internal vibrational modes of CH_3Cl.

Below the threshold energy, the present experiments indicate the reaction probability is smaller than indicated by previous flow/drift tube results,[7] although the present measurements are not definitive at near-thermal energies. It is possible that the discrepancies can be explained by buffer gas collision effects.

There is a significant secondary kinetic isotope effect. The translationally activated reaction is about 20% faster for CH_3Cl than for CD_3Cl. On the basis of density of states arguments, this is consistent with a competition between the S_N2 reaction and decomposition back to reactants. The latter is much more likely overall for any collision complex or random collision encounter, and the increase in the densities of states for the deuterated system differentially favors decomposition back to reactants over crossing the transition-state barrier. Tunneling may also contribute by allowing the hydrogen system to cut corners on the potential energy surface.

Simple statistical models cannot account for the elevated threshold for translational activation or for the energy dependence of the kinetic isotope effect. It is possible that statistical models with more accurate treatment of angular momentum and anharmonicity would do better. Nevertheless, the present results reinforce the picture from the trajectory calculations of Hase and co-workers[2,12,14−18] that the reaction is nonstatistical in nature. Nonstatistical effects have also been found experimentally for other halide/halomethane S_N2 reactions, for example in the $Cl^- + CH_3Br$ reaction.[11,37,124,130] It has been suggested[131] that nonstatistical behavior for these simple halide/halomethane S_N2 reactions is a consequence of the very short lifetimes of the ion−dipole complexes, while larger systems or those with deeper wells have complex lifetimes long enough to exchange energy statistically. Thus, the complicated behavior found in the gas phase for the "simple" S_N2 reactions of halomethanes (eq 1) may not be entirely representative of bimolecular nucleophilic substitution reactions in general.

Acknowledgment. We thank Veronica M. Bierbaum for discussions and for providing data from previous work.[7] We would like to thank Peter B. Armentrout, Paul R. Kemper, Doreen G. Leopold, Richard A. Schaeffer, and Petra A. M. van Koppen for helpful discussions and suggestions. Alexander Grushow, Taeck-Hong Lee, and Vassil A. Spasov assisted in the construction and development of the GIB-MS instrument. The machining skills of Walter Weaver are appreciated. This work was supported by National Science Foundation Grant CHE-9423326 and cooperative agreement OSR-9353227. Acknowledgment is also made to the donors of the Petroleum Research Fund, administered by the American Chemical Society, for partial support of this research.

References and Notes

(1) Shaik, S. S.; Schlegel, H. B.; Wolfe, S. *Theoretical Aspects of Physical Organic Chemistry: The S_N2 Mechanism*; John Wiley and Sons, Inc.: New York, 1992.
(2) Hase, W. L. *Science* **1994**, *266*, 998−1002.
(3) Olmstead, W. N.; Brauman, J. I. *J. Am. Chem. Soc.* **1977**, *99*, 4219−4228.
(4) Brauman, J. I. *J. Mass Spectrom.* **1995**, *30*, 1649−1650.
(5) Dodd, J. A.; Brauman, J. I. *J. Phys. Chem.* **1986**, *90*, 3559−3562. [See ref 14].
(6) Van Doren, J. M.; DePuy, C. H.; Bierbaum, V. M. *J. Phys. Chem.* **1989**, *93*, 1130−1134.
(7) Barlow, S. E.; Van Doren, J. M.; Bierbaum, V. M. *J. Am. Chem. Soc.* **1988**, *110*, 7240−7242.
(8) Tucker, S. C.; Truhlar, D. G. *J. Phys. Chem.* **1989**, *93*, 8138−8142.
(9) Tucker, S. C.; Truhlar, D. G. *J. Am. Chem. Soc.* **1990**, *112*, 3338−3347.
(10) Wladkowski, B. D.; Brauman, J. I. *J. Phys. Chem.* **1993**, *97*, 13158−13164.
(11) Graul, S. T.; Bowers, M. T. *J. Am. Chem. Soc.* **1994**, *116*, 3875−3883.
(12) Vande Linde, S. R.; Hase, W. L. *J. Am. Chem. Soc.* **1989**, *111*, 2349−2351.
(13) Vande Linde, S. R.; Hase, W. L. *J. Phys. Chem.* **1990**, *94*, 2778−2788.
(14) Vande Linde, S. R.; Hase, W. L. *J. Chem. Phys.* **1990**, *93*, 7962−7980.
(15) Vande Linde, S. R.; Hase, W. L. *J. Phys. Chem.* **1990**, *94*, 6148−6150.
(16) Cho, Y. J.; Vande Linde, S. R.; Zhu, L.; Hase, W. L. *J. Chem. Phys.* **1992**, *96*, 8275−8287.
(17) Hase, W. L.; Cho, Y. J. *J. Chem. Phys.* **1993**, *98*, 8626−8639.
(18) Peslherbe, G. H.; Wang, H.; Hase, W. L. *J. Chem. Phys.* **1995**, *102*, 5626−5635.
(19) Shaik, S. S.; Pross, A. *J. Am. Chem. Soc.* **1982**, *104*, 2708−2719.
(20) Chandrasekhar, J.; Smith, S. F.; Jorgensen, W. L. *J. Am. Chem. Soc.* **1985**, *107*, 154−163.
(21) Shi, Z.; Boyd, R. J. *J. Am. Chem. Soc.* **1989**, *111*, 1575−1579.
(22) Shi, Z.; Boyd, R. J. *J. Am. Chem. Soc.* **1990**, *112*, 6789−6796.
(23) Vetter, R.; Zülicke, L. *J. Am. Chem. Soc.* **1990**, *112*, 5136−5142.
(24) Wladkowski, B. D.; Lim, K. F.; Allen, W. D.; Brauman, J. I. *J. Am. Chem. Soc.* **1992**, *114*, 9136−9153.
(25) Truong, T. N.; Sefanovich, E. V. *J. Phys. Chem.* **1995**, *99*, 14700−14706.
(26) Glukhovtsev, M. N.; Pross, A.; Radom, L. *J. Am. Chem. Soc.* **1995**, *117*, 2024−2032.
(27) Glukhovtsev, M. N.; Pross, A.; Schlegel, H. B.; Bach, R. D.; Radom, L. *J. Am. Chem. Soc.* **1996**, *118*, 11258−11264.
(28) Deng, L.; Branchadell, V.; Ziegler, T. *J. Am. Chem. Soc.* **1994**, *116*, 10645−10656.
(29) Billing, G. D. *Chem. Phys.* **1992**, *159*, 109−126.
(30) Clary, D. C.; Palma, J. *J. Chem. Phys.* **1997**, *106*, 575−583.
(31) White, N. R.; Scott, D.; Huq, M. S.; Doverspike, L. D.; Champion, R. L. *J. Chem. Phys.* **1984**, *80*, 1108−1115.
(32) Zellermann, G.; Vietzke, E. *Radiochem. Acta* **1990**, *50*, 107−115.
(33) Zhao, X. G.; Tucker, S. T.; Truhlar, D. G. *J. Am. Chem. Soc.* **1991**, *113*, 826−832.
(34) Gonzalez-Lafont, A.; Truong, T. N.; Truhlar, D. G. *J. Phys. Chem.* **1991**, *95*, 4618−4627.
(35) Zhao, X. G.; Lu, D.-H.; Liu, Y.-P.; Lynch, G. C.; Truhlar, D. G. *J. Chem. Phys.* **1992**, *97*, 6369−6383.
(36) Viggiano, A. A.; Paschkewitz, J. S.; Morris, R. A.; Paulson, J. F.; Gonzalez-Lafont, A.; Truhlar, D. G. *J. Am. Chem. Soc.* **1991**, *113*, 9404−9405.
(37) Viggiano, A. A.; Morris, R. A.; Paschkewitz, J. S.; Paulson, J. F. *J. Am. Chem. Soc.* **1992**, *114*, 10477−10482.
(38) O'Hair, R. A.; Davico, G. E.; Hacaloglu, J.; Dang, T. T.; DePuy, C. H.; Bierbaum, V. M. *J. Am. Chem. Soc.* **1994**, *116*, 3609−3610.
(39) Dougherty, R. C.; Dalton, J.; Roberts, J. D. *Org. Mass Spectrom.* **1977**, *8*, 77−79.
(40) Li, C.; Ross, P.; Szulejko, J. E.; McMahon, T. B. *J. Am. Chem. Soc.* **1996**, *118*, 9360−9367.
(41) Larson, J. W.; McMahon, T. B. *J. Am. Chem. Soc.* **1984**, *106*, 517−521.
(42) Larson, J. W.; McMahon, T. B. *J. Am. Chem. Soc.* **1985**, *107*, 766−773.
(43) Grushow, A.; Ervin, K. M. *J. Am. Chem. Soc.* **1995**, *117*, 11612−11613.
(44) Grushow, A.; Ervin, K. M. *J. Chem. Phys.* **1997**, *106*, 9580−9593.
(45) Ervin, K. M.; Armentrout, P. B. *J. Chem. Phys.* **1985**, *83*, 166−189.
(46) Hanley, L.; Ruatta, S. A.; Anderson, S. L. *J. Chem. Phys.* **1987**, *87*, 260−268.
(47) Ray, U.; Jarrold, M. F.; Bower, J. E.; Kraus, J. S. *J. Chem. Phys.* **1989**, *91*, 2912−2921.
(48) Dressler, R. A.; Salter, R. H.; Murad, E. *J. Chem. Phys.* **1993**, *99*, 1159−1171.
(49) Ichihashi, M.; Hirokawa, J.; Nonose, S.; Nagata, T.; Kondow, T. *Chem. Phys. Lett.* **1993**, *204*, 219−225.

(50) Mark, S.; Schellhammer, C.; Niedner-Schatteburg, G.; Gerlich, D. *J. Phys. Chem.* **1995**, *99*, 15587−15594.
(51) Graul, S. T.; Squires, R. R. *Mass Spectrom. Rev.* **1988**, *7*, 263−358.
(52) Ferguson, E. E.; Fehsenfeld, F. C.; Schmeltekopf, A. L. *Adv. At. Mol. Phys.* **1969**, *5*, 1−56.
(53) Ren, X.; Hintz, P. A.; Ervin, K. M. *J. Chem. Phys.* **1993**, *99*, 3575−3587.
(54) Hintz, P. A.; Ervin, K. M. *J. Chem. Phys.* **1994**, *100*, 5715−5725.
(55) Lee, T. H.; Ervin, K. M. *J. Phys. Chem.* **1994**, *98*, 10023−10031.
(56) Hintz, P. A.; Ervin, K. M. *J. Chem. Phys.* **1995**, *103*, 7897−7906.
(57) Leopold, D. G.; Ho, J.; Lineberger, W. C. *J. Chem. Phys.* **1987**, *86*, 1715−1726.
(58) Ho, J.; Ervin, K. M.; Lineberger, W. C. *J. Chem. Phys.* **1990**, *93*, 6987−7002.
(59) Fehsenfeld, F. C.; Evenson, K. M.; Broida, H. P. *Rev. Sci. Instrum.* **1965**, *36*, 294−298.
(60) Leopold, D. G.; Murray, K. K.; Stevens Miller, A. E.; Lineberger, W. C. *J. Chem. Phys.* **1985**, *83*, 4849−4865.
(61) Heddle, D. W. O. *J. Phys. E.* **1971**, *4*, 981−983.
(62) Giese, C. F. *Rev. Sci. Instrum.* **1959**, *30*, 260−261.
(63) Lu, C.-S.; Carr, H. E. *Rev. Sci. Instrum.* **1962**, *33*, 823−833.
(64) Denison, D. R. *J. Vac. Sci. Technol.* **1971**, *8*, 266−269.
(65) Zeman, H. D. *Rev. Sci. Instrum.* **1977**, *48*, 1079−1085.
(66) Farley, J. W. *Rev. Sci. Instrum.* **1985**, *56*, 1834−1835.
(67) Plastridge, B.; Cohen, M. H.; Cowen, K. A.; Wood, D. A.; Coe, J. V. *J. Phys. Chem.* **1995**, *99*, 118−122.
(68) Dahl, D. A.; Delmore, J. E. SIMION; Vers. 4.02; Idaho Falls: Idaho National Engineering Laboratory, 1989.
(69) Herzog, R. *Z. Phys.* **1935**, *97*, 596−602.
(70) Jost, K. *J. Phys. E: Sci. Instrum.* **1979**, *12*, 1001−1005.
(71) Pollard, J. E.; Trevor, D. J.; Lee, Y. T.; Shirley, D. A. *Rev. Sci. Instrum.* **1981**, *52*, 1837−1846.
(72) Ballu, P. Y. *Rev. Phys. Appl.* **1968**, *3*, 46−52.
(73) Bernius, M. T.; Chufjian, A. *Rev. Sci. Instrum.* **1989**, *60*, 779−782.
(74) Bernius, M. T.; Chufjian, A. *Rev. Sci. Instrum.* **1990**, *61*, 925−927.
(75) Gerlich, D. *Adv. Chem. Phys.* **1992**, *82*, 1−176.
(76) Ervin, K. M. Ph.D. Dissertation, University of California, Berkeley, 1986.
(77) Pedder, R. E.; Schaeffer, R. A., *Proceedings*, 43rd ASMS Conference on Mass Spectrometry and Allied Topics, Atlanta, GA, 1995; p 1069.
(78) Grimm, C. C.; Clawson, R.; Short, R. T. *J. Am. Soc. Mass Spectrom.* **1997**, *8*, 539−544.
(79) Levandier, D. J.; Dressler, R. A.; Murad, E. *Rev. Sci. Instrum.* **1997**, *68*, 64−69.
(80) Lian, L.; Su, C.-X.; Armentrout, P. B. *J. Chem. Phys.* **1992**, *97*, 4072−4083.
(81) Bevington, P. R. *Data Reduction and Error Analysis for the Physical Sciences*; McGraw-Hill: New York, 1969.
(82) Khan, F. A.; Clemmer, D. E.; Schultz, R. H.; Armentrout, P. B. *J. Phys. Chem.* **1993**, *97*, 7978−7987.
(83) Armentrout, P. B.; Hales, D. A.; Lian, L. In *Advances in Metal and Semiconductor Clusters*; Duncan, M. A., Eds.; JAI Press: Greenwich, CT, 1994; Vol. 2, pp 1−39.
(84) Sunderlin, L. S.; Wang, D.; Squires, R. R. *J. Am. Chem. Soc.* **1993**, *115*, 12060−12070.
(85) Levine, R. D.; Bernstein, R. B. *Chem. Phys. Lett.* **1971**, *11*, 552−536.
(86) Levine, R. D.; Bernstein, R. B. *J. Chem. Phys.* **1972**, *56*, 2281−2287.
(87) Rebick, C.; Levine, R. D. *J. Chem. Phys.* **1973**, *58*, 3942−3952.
(88) Chesnavich, W. J.; Bowers, M. T. *J. Chem. Phys.* **1978**, *68*, 901−903.
(89) Chesnavich, W. J.; Bowers, M. T. *J. Phys. Chem.* **1979**, *83*, 900−905.
(90) Loh, S. K.; Hales, D. A.; Lian, L.; Armentrout, P. B. *J. Chem. Phys.* **1989**, *90*, 5466−5485.
(91) Levine, R. D.; Bernstein, R. B. *Molecular Reaction Dynamics and Chemical Reactivity*; Oxford University Press: New York, 1987.
(92) Smith, I. W. M. *J. Chem. Educ.* **1982**, *59*, 9−14.
(93) Rodgers, M. T.; Ervin, K. M.; Armentrout, P. B. *J. Chem. Phys.* **1997**, *106*, 4499−4508.
(94) Armentrout, P. B. In *Structure/Reactivity and Thermochemistry of Ions*; Ausloos, P.; Lias, S. G., Eds.; Reidel: Dordrecht, 1987; pp 97−164.
(95) Beyer, T. S.; Swinehart, D. F. *Commun. ACM* **1973**, *16*, 379.
(96) Stein, S. E.; Rabinovitch, B. S. *J. Chem. Phys.* **1973**, *58*, 2438−2445.
(97) Stein, S. E.; Rabinovitch, B. S. *Chem. Phys. Lett.* **1977**, *49*, 183−188.
(98) Chantry, P. J. *J. Chem. Phys.* **1971**, *55*, 2746−2759.
(99) Lifshitz, C.; Wu, R.; Tiernan, T. O.; Terwilleger, D. T. *J. Chem. Phys.* **1978**, *68*, 247−260.
(100) Gerlich, D. *J. Chem. Phys.* **1989**, *90*, 127−139.
(101) Demas, J. N. *Excited-State Lifetime Measurements*; Academic: New York, 1983; p 98.
(102) Armentrout, P. B.; Ervin, K. M. Crunch; FORTRAN program, 1996.
(103) Herzberg, G. *Molecular Spectra and Molecular Structure II. Infrared and Raman Spectra of Polyatomic Molecules*; Van Nostrand Reinhold: New York, 1945.
(104) Albritton, D. L.; Dotan, I.; Lindinger, W.; McFarland, M.; Tellinghuisen, J.; Fehsenfeld, F. C. *J. Chem. Phys.* **1977**, *66*, 410−421.
(105) Viehland, L. A.; Mason, E. A.; Whealton, J. H. *J. Phys. B: Atom. Mol. Phys.* **1974**, *7*, 2433−2439.
(106) Viehland, L. A.; Mason, E. A. *J. Chem. Phys.* **1977**, *66*, 422−434.
(107) Viehland, L. A.; Kirkpatrick, C. C. *Int. J. Mass Spectrom. Ion Proc.* **1995**, *149/150*, 555−571.
(108) Koutselos, A. D.; Mason, E. A.; Viehland, L. A. *J. Chem. Phys.* **1990**, *93*, 7125−7136.
(109) Chesnavich, W. J.; Bowers, M. T. *J. Am. Chem. Soc.* **1976**, *98*, 8301−8309.
(110) Chesnavich, W. J.; Bowers, M. T. *J. Chem. Phys.* **1977**, *66*, 2306−2315.
(111) Weber, M. E.; Dalleska, N. F.; Tjelta, B. L.; Fisher, E. R.; Armentrout, P. B. *J. Chem. Phys.* **1993**, *98*, 7855−7867.
(112) Grice, M. E.; Song, K.; Chesnavich, W. J. *J. Phys. Chem.* **1986**, *90*, 3503−3509.
(113) Lias, S. G.; Bartmess, J. E.; Liebman, J. F.; Holmes, J. L.; Levin, R. D.; Mallard, W. G. *J. Phys. Chem. Ref. Data* **1988**, *17* (Suppl. 1).
(114) Frisch, M. J.; Trucks, G. W.; Schlegel, H. B.; Gill, P., et al. Gaussian94; Revision D.4; Gaussian, Inc.: Pittsburgh, PA, 1995.
(115) Scott, A. P.; Radom, L. *J. Phys. Chem.* **1996**, *100*, 16502−16513.
(116) Giles, K.; Grimsrud, E. P. *J. Phys. Chem.* **1992**, *96*, 6680−6687.
(117) Knighton, W. B.; Bognar, J. A.; O'Conner, P. M.; Grimsrud, E. P. *J. Am. Chem. Soc.* **1993**, *115*, 12079−12084.
(118) Seeley, J. V.; Morris, R. A.; Viggiano, A. A.; Want, H.; Hase, W. L. *J. Am. Chem. Soc.* **1997**, *119*, 577−584.
(119) Sahlstrom, K. E.; Knighton, W. B.; Grimsrud, E. P. *J. Phys. Chem. A* **1997**, *101*, 1501−1508.
(120) Kabbaj, O. K.; Lepetit, M. B.; Malrieu, J. P.; Sini, G.; Hiberty, P. C. *J. Am. Chem. Soc.* **1991**, *113*, 5619−5627.
(121) VanOrden, S. L.; Pope, R. M.; Buckner, S. W. *Org. Mass Spectrom.* **1991**, *26*, 1003−1007.
(122) Cyr, D. M.; Bailey, C. G.; Serxner, D.; Scarton, M. G.; Johnson, M. A. *J. Chem. Phys.* **1994**, *101*, 10507−10520. Dessent, C. E. H.; Johnson, M. A. *J. Am. Chem. Soc.* **1997**, *119*, 5067−5068.
(123) Okuno, Y. *J. Chem. Phys.* **1996**, *105*, 5817−5829.
(124) Viggiano, A. A.; Morris, R. A. *J. Phys. Chem.* **1996**, *100*, 19227−19240.
(125) Gronert, S.; DePuy, C. H.; Bierbaum, V. M. *J. Am. Chem. Soc.* **1991**, *113*, 4009−4010.
(126) Miller, W. H. *J. Chem. Phys.* **1976**, *65*, 2216−2223.
(127) Chesnavich, W. J.; Bowers, M. T. *Prog. React. Kinet.* **1982**, *11*, 137−267.
(128) Hirao, K.; Kebarle, P. *Can. J. Chem.* **1989**, *67*, 1261−1267.
(129) Cyr, D. A.; Scarton, M. G.; Wiberg, K. B.; Johnson, M. A.; Nonose, S.; Hirokawa, J.; Tanaka, H.; Kondow, T.; Morris, R. A.; Viggiano, A. A. *J. Am. Chem. Soc.* **1995**, *117*, 1828−1832.
(130) Graul, S. T.; Bowers, M. T. *J. Am. Chem. Soc.* **1991**, *113*, 9696−9697.
(131) Viggiano, A. A.; Morris, R. A.; Su, T.; Wladkowski, B. D.; Craig, S. L.; Zhong, M.; Brauman, J. I. *J. Am. Chem. Soc.* **1994**, *116*, 2213−2214.